Acta Universitatis
Lappeenrantaensis
840

Denys Musiienko

Ni-Mn-Ga MAGNETIC SHAPE MEMORY ALLOY FOR PRECISE HIGH-SPEED ACTUATION IN MICRO-MAGNETO-MECHANICAL SYSTEMS

Denys Musiienko

Ni-Mn-Ga MAGNETIC SHAPE MEMORY ALLOY FOR PRECISE HIGH-SPEED ACTUATION IN MICRO-MAGNETO-MECHANICAL SYSTEMS

Thesis for the degree of Doctor of Science (Technology) to be presented with due permission for public examination and criticism in the Lecture Hall 1314 at LUT University, Lappeenranta, Finland on the 17th of January, 2019, at noon.

Acta Universitatis
Lappeenrantaensis 840

Supervisor Professor Kari Ullakko
LUT School of Engineering Science
LUT University
Finland

Reviewers Dr. Ilkka Aaltio
Department of Materials Science and Engineering
Aalto University
Finland

Asst. Prof. Markus Chmielus
Mechanical Engineering & Materials Science
University of Pittsburgh
USA

Opponent Prof. Dr. Manfred Kohl
Institute of Microstructure Technology
Karlsruhe Institute of Technology
Germany

ISBN 978-952-335-334-3
ISBN 978-952-335-335-0 (PDF)
ISSN-L 1456-4491
ISSN 1456-4491

LUT-yliopisto
LUT Yliopistopaino 2019

Abstract

Denys Musiienko

Ni-Mn-Ga magnetic shape memory alloy for precise high-speed actuation in micro-magneto-mechanical systems

Lappeenranta 2019
56 pages
Acta Universitatis Lappeenrantaensis 840
Diss. LUT University
ISBN 978-952-335-334-3, ISBN 978-952-335-335-0 (PDF)
ISSN-L 1456-4491, ISSN 1456-4491

Single crystalline Ni-Mn-Ga alloys are known for their large reversible magnetic-field-induced strain (MFIS) of several percent. This effect was discovered and named magnetic shape memory (MSM) by K. Ullakko in 1996. Since then it has been exciting scientific minds with its amazing properties and hidden potential. The mechanism behind the MSM effect is the magnetically induced reorientation (MIR) of the crystal lattice in martensite phase. Martensitic twin variants with the short crystallographic c-axis (axis of easy magnetization) oriented along the applied magnetic field grow at the expense of other variants with different orientation. Despite numerous studies devoted to bulk Ni-Mn-Ga elements, the research on the behavior of the MSM materials at microscale is limited.

This Thesis presents the attempt to fabricate MSM microdevice by using top-down approach, i. e. decreasing the dimensions of a bulk Ni-Mn-Ga single crystal with defined composition and known properties. The possibility of MIR in Ni-Mn-Ga foils thinned down to 1 μm was revealed. Prototyping technology (based on FIB milling and electro-chemical etching) for MSM microdevices was developed and used for fabrication of the micropillars. Difference in dynamics of type I and type II twin boundaries at the microscale was found. The measured actuation velocities of 0.18 and 1.3 (m/s) for type I and type II TBs correspond strongly with the previously reported values for bulk, mm-sized samples. The actuation acceleration of micropillars was found to be approximately an order of magnitude larger than in bulk samples, demonstrating a well-pronounced scaling effect connected to the decrease of cross-section in actuated MSM crystals and therefore the reduction of moving mass. Twinning stresses for single twin boundaries motion in micropillars were revealed to be $\sim$ 2.3 MPa for type I twins and $\sim$ 0.8 MPa for type II. It is suggested that increased twinning stress values (in comparison to the values for bulk material) are related to the incomplete removal of surface defects, but this issue requires further investigation. It was demonstrated that in micropillars giant MFIS of more than 6 % can be obtained in about 5 μs.

The results presented in the Thesis suggest the possibility of fabricating MSM-based microdevices with bandwidth of 10^5 Hz, which is an order higher than previously reported.

Keywords: magnetic shape memory alloy, ferromagnetic shape memory, twinning, magnetic domains, Ni-Mn-Ga, nanoindentation, focused ion beam, twin boundary kinetics, micropillars

Acknowledgements

The Thesis includes the research carried out in Prof. Kari Ullakko's Material Physics Laboratory at LUT University, Savonlinna, Finland, during 2015 – 2018 years. The financial support from the Finnish Academy of Sciences (grant numbers 277996 and 287016) is greatly acknowledged.

I first encountered Ni-Mn-Ga alloys in 2008, when I was employed as junior engineer at Institute for Metal Physics (IMP) in Kyiv, Ukraine. Back then I was studying applied physics at National Aviation University. This was the very start of my very personal relationship with this exciting extraordinary material. In 2012, I finished my Master's degree at Kyiv's department of Moscow Institute of Physics and Technology (State University) that was based on the same Institute for Metal Physics I was working at. My Master's degree supervisor was Dr. Nadiya Glavatska, who introduced me to the magnetic shape memory research field. I am very grateful to all highly skilled docents, professors and academicians who devoted their priceless time to my education during my studies and scientific work at IMP.

Later in 2013 I met Prof. Kari Ullakko and Dr. Aaron Smith at the ICFM 2013 conference. They did blow my mind with their breakthrough studies on the MSM single crystals and we negotiated my research visit to their newly established Material Physics Laboratory in 2014. During that research stay I was introduced to various internal workings like "magic bamboo stick" and how to use it to create different types of twinning interfaces in single crystalline Ni-Mn-Ga. When my research stay came to an end, Doctor (back then) Kari Ullakko made me an offer which I could not refuse: doctoral studies application under his supervision. This was a life-changing opportunity for me and I'm very grateful to him for it.

I am particularly grateful to Olli Mattila for sharing his knowledge about vacuum systems and crystal growth techniques. I thank Dr. Juhani Tellinen for great discussions about theoretical basis of my research. I had the pleasure to work with Dr. Oleksii Sozinov who is a known expert in MSM field. I enjoyed carrying out experiments and writing scientific reports with Dr. Andrey Saren. I appreciate the expertise in materials mechanical treatment constantly provided by Janne Huimasalo when I had a need to create a custom experimental apparatus. I am especially grateful to Dr. Ladislav Straka and Dr. Oleg Heczko who supported my research ambitions during the late stage of my doctoral studies.

Thank you all, my colleagues and friends, without you this Thesis would have never been completed.

Denys Musiienko
September 2018
Savonlinna, Finland

To my family and friends

Contents

List of publications

This thesis contains material from the following papers. The rights have been granted by publishers to include the material in dissertation.

I. Musiienko, D., Saren, A., Ullakko, K. (2017). Magnetic shape memory effect in single crystalline Ni-Mn-Ga foil thinned down to 1 μm. *Scripta Materialia*, 139, pp. 152–154.

II. Musiienko, D., Straka, L., Klimša, L., Saren, A., Sozinov, A., Heczko, O., Ullakko, K. (2018). Giant magnetic-field-induced strain in Ni-Mn-Ga micropillars. *Scripta Materialia*, 150, pp. 173–176

III. Musiienko, D., Straka, L., Klimša, L., Saren, A., Sozinov, A., Heczko, O., Ullakko, K. (2018). Magnetic-field-induced actuation of Ni-Mn-Ga micro-pillars. *Proceedings of 16th International Conference on New Actuators "ACTUATOR2018"*, pp. 229–231

IV. Musiienko, D., Saren, A., Straka, L., Vronka, M., Kopeček, J., Heczko, O., Sozinov, A., Ullakko, K., Ultrafast actuation of Ni-Mn-Ga micropillars by pulsed magnetic field. *Scripta Materialia*, 162, pp. 482–485

Author's Contribution

The Author was responsible for, planned the research and carried out the major part of experimental investigations in **Publications I – III**. **Publication IV** is a joint effort of the Author and Dr. Andrey Saren, who developed the high-speed magnetic actuation experimental apparatus. All publications were being discussed with co-authors during their preparation.

Prof. Kari Ullakko supervised and mentored me throughout the whole research path. Dr. Andrey Saren was responsible for atomic and magnetic force microscopy measurements in **Publications I – III**. Dr. Ladislav Straka and Dr. Oleg Hezcko provided their expertise and supervised the Author during multiple research visits the to Institute of Physics of the Czech Academy of Sciences. They participated in preparation of **Publications II – IV**. Dr. Oleksii Sozinov supplied high-quality Ni-Mn-Ga single crystals for the experiments carried out in all publications and supported the Author by sharing his extensive knowledge of the research field. Mr. Ladislav Klimša operated TESCAN FERA3 scanning electron microscope with integrated electron-cyclotron-resonance-generated Xe plasma focused ion beam milling and machined micropillars for **Publications II – IV**. Dr. Marek Vronka was responsible for conducting compressive stress measurements presented in **Publication IV**.

The results of **Publication IV** were presented at the 11th European Symposium on Martensitic Transformations ESOMAT2018. The Author received Best Poster Award for the poster entitled "High-speed actuation of Ni-Mn-Ga micropillars by pulsed magnetic field".

Nomenclature

Abbreviations

10M	10-layered martensite lattice, also referred as 5M
14M	14-layered martensite lattice, also referred as 7M
1D	one-dimensional
2D	two-dimensional
3D	three-dimensional
AFM	atomic force microscope
ETD	Everhart–Thornley SE detector
FIB	focused ion beam
LDV	laser Doppler vibrometer
MD	magnetic domain
MEMS	microelectromechanical system
MFIS	magnetic-field-induced strain
MFM	magnetic force microscopy
MIR	magnetically induced reorientation
MMMS	micromagnetomechanical system
MP	micropillar
MSM	magnetic shape memory
PID	proportional-integral-derivative (controller)
PWM	pulse width modulation
RT	room temperature
SC	single crystal
SE	secondary electrons
SEM	scanning electron microscope
SMA	shape memory alloy
TB	twin boundary
TS	twinning stress

Greek Symbols

β	angle of the spatial orientation deviation between two twin variants	$^\circ$
δ	characteristic width of magnetic domains	µm
γ	monoclinic crystallographic cell angle	$^\circ$
σ	applied mechanical stress	MPa
σ_1	dynamic TS for type I TB	MPa
σ_2	dynamic TS for type II TB	MPa
σ_{mag}	magnetic-field-induced stress	MPa
σ_{res}	resistance stress	MPa
σ_{tw}	twinning stress	MPa
ε_0	maximum strain of the crystal	

Roman Symbols

$\boldsymbol{F}$	driving force	N
$\boldsymbol{H}$	magnetic field vector	A/m
a, b	long hard magnetisation axes	nm
A_0	cross-section of the micropillar	m^2
c	short easy magnetisation axis	nm
E_0	energy terms not included in U_k, E_{tw} and W	J
E_{tw}	energy required for TB motion	J

H_{min}	minimal magnetic field required for MIR	kA/m
H_{sat}	saturation magnetic field for MSM material	kA/m
L	TB position measured along [001] direction	m
L_0	initial position of the TB	m
m_0	initial mass of the moving variant	µg
t	time variable	s
T_A	austenite transformation temperature	K
T_C	Curie temperature	K
T_M	martensite transformation temperature	K
U_k	magnetic anisotropy energy	J
V_E	elongation velocity	m/s
V_{TB}	TB propagation velocity	K
W	work performed by actuation	J

1 Introduction

Ni-Mn-Ga off-stoichiometric Heusler compounds are known for their large reversible magnetic-field-induced strain (MFIS) of several percent. The effect was discovered and named magnetic shape memory (MSM) by K. Ullakko in 1996, and since then it has been exciting scientific minds with its hidden potential and properties (Ullakko, 1996; Murray et al., 2000; Faran and Shilo, 2016). The mechanism behind the MSM effect is the magnetically induced reorientation (MIR) of the crystal lattice in martensite phase. Martensitic twin variants with the short crystallographic c-axis (axis of easy magnetization) oriented along the applied magnetic field grow at the expense of other variants with different orientation (Aaltio et al., 2016). After the magnetic field is removed, the specimen retains its shape.

So far, the main interest in MSM alloys comes from actuation applications in which these materials provide unique capabilities that cannot be obtained by other actuation mechanisms (Faran and Shilo, 2016). One of the most advantageous directions of the MSM-based applications development is the actuation at micro-scale (Nespoli et al., 2010). The MSM element size decrease will lead to the decrease of its mass, which in turn will lead to the increase of operating frequency. However, in (Arzt, 1998), large change of mechanical properties was predicted when the smallest dimension of a sample becomes comparable to the characteristic length relevant for the dislocation-mediation mechanism which has an order of a micrometer. According to Dunand and Müllner, twinning is a disconnection-mediated process, which resembles in many ways dislocation-mediated processes, and its characteristic length is assumed to be of a similar order (Dunand and Müllner, 2011). They expect an increase of the twinning stress with decreasing characteristic size (i.g. foil thickness) which would hinder MFIS.

The first problem that is being solved in this work is related to the size limitations of MSM effect. The challenges connected with development and fabrication of Ni-Mn-Ga microdevices will be revealed and solved. In this Thesis two common techniques, electrochemical etching and nanoindentation, are modified and applied in an unusual way. Modern electron-cyclotron-resonance-generated Xe plasma focused ion beam milling technology is used for prototyping of simple microactuator. Laser Doppler vibrometry is being employed to measure the mechanical response of micropillar to a magnetic field pulse application. Fast camera imaging will be used for real-time observation of the behavior of the MSM microdevice under exposure to magnetic fields.

The "State of the art" chapter gives a short introduction into the magnetic shape memory field. Chapter 3 reveals objectives and plan of the research, that evolved during the progression of the present study to accommodate new findings and concepts. Chapter 4 "Methods" provides an overview of scientific techniques and methods that were developed and/or used in the Thesis. Chapter 5 presents and discusses original results obtained in this work. Conclusions and future research plans are summarized in Chapter 6.

2 State of the art

This chapter presents general information about the material properties of Ni-Mn-Ga alloys. It is intended to introduce a general reader into magnetic shape memory field and support understanding of the results discussed in the Thesis.

2.1 Crystal structure of Ni-Mn-Ga alloys

A detailed study of magnetic order and phase transformation in stoichiometric $Ni_{50}Mn_{25}Ga_{25}$ was performed by Webster et al. (1984). The melting temperature of Ni_2MnGa alloys is about 1350 K. Upon cooling the liquid forms directly a B2′ phase. The B2′ transition to highly ordered, Heusler type ($L2_1$), structure occurs at 1071 K in stoichiometric Ni_2MnGa within a short time (Overholser et al., 1999). A stoichiometric $Ni_{50}Mn_{25}Ga_{25}$ alloy exhibits cubic $L2_1$ crystal structure at RT with lattice parameter $a = 0.5825$ nm (see Figure 2.1). Ni ions occupy the corner sites of the body-centered cubic structure, while Mn and Ga ions occupy alternate body-center sites. The high temperature parent phase will further transform to martensite with a lower symmetry at decreasing temperature. The composition variation of the Ni-Mn-Ga compound near stoichiometric proportions results in a change of the martensitic transformation temperature (T_M) ranging from 160 to 450 K (Vasil′ev et al., 1999). The product of this transformation has been identified by X-ray diffraction as modulated tetragonal martensite with lattice parameters $a = b = 0.5925$ nm and $c = 0.5263$ nm (Ma et al., 2000).

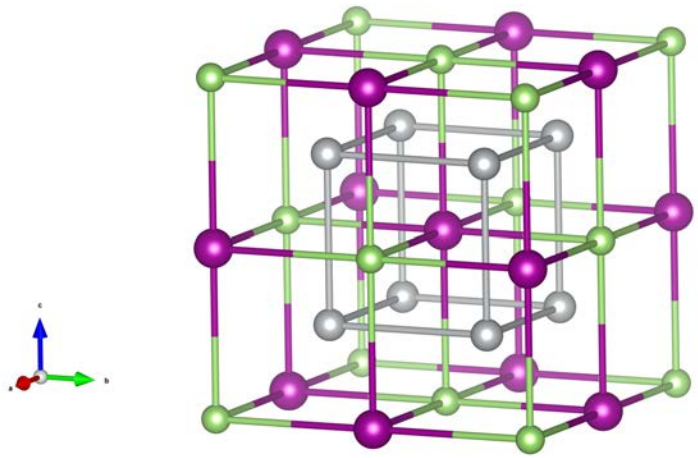

Figure 2.1: The FFC $L2_1$ structure of stoichiometric Ni_2MnGa at RT. Nickel atoms are grey, manganese atoms are velvet and gallium atoms are green.

Additionally the alloy undergoes a ferromagnetic transformation in austenitic phase with the Curie temperature (T_C) located at the range of 300–400 K for the variety of studied compositions, for the stoichiometric composition $T_C = 376K$ (Aaltio et al., 2016). The temperatures of

ferromagnetic and martensitic transitions were found to be quite sensitive to distances between Mn ions. The application of external pressure such as hydrostatic, compression and magnetic field can lead to the shifting of the T_M and T_C (Vasil′ev et al., 1999; Ma et al., 2000). Large strains caused by the martensitic transformation are accommodated by crystallographic twinning. The different martensitic twin variants have the same primitive cell but different structural orientation (Lanska et al., 2004).

Three different martensitic phases are generally distinguished in Ni-Mn-Ga compounds (Heczko et al., 2009; Aaltio et al., 2016). Five-layered modulated martensite (usually referred to as 5M or 10M) is described by monoclinic cell with $a \simeq b$, $c < a$ and $\gamma > 90°$, being modulated over 10 (220) atomic planes along $[\bar{1}10]$ direction. In seven-layered modulated martensite (named 7M or 14M) original cubic cell is distorted being orthorhombic with $a > b > c$, modulation over 14 (220) atomic planes along $[\bar{1}10]$ direction. The confusion between the 5M or 10M and 7M or 14M is resolved by counting modulation layers in unit cells or atomic plains. In the current work we will keep naming modulated martensites as 5M and 7M. Non-modulated (NM) martensite has tetragonal crystal structure with $a = b$ and $c > a$, with no modulation. The maximum possible compressive strain in the single crystalline martensite can be described by the tetragonal distortion of the lattice $\varepsilon_0 = 1 - c/a$ (Söderberg et al., 2005). Most of the observations of the MSM effect have been done for five-layered martensite, including the present study.

2.2 Twinning

Jaswon and Dove (1960) characterised twinned crystals by four crystallographic elements symbolised as K_1, K_2, ν_1 and ν_2 together with two subsidiary elements P and λ, as illustrated in Figure 2.2 and listed below:

K_1 : twin plane.
K_1 : "second undistorted" plane.
P : plane of shear (perpendicular to K_1, K_2 and λ)
ν_1 : line of intersection of P, K_1.
ν_2 : line of intersection of P, K_2.
λ : line of intersection of K_1, K_2.

Twin variants can be classified into compound (mirrored symmetry, K_1, K_2, ν_1 and ν_2 are rational) and non-compound (Bhattacharya et al., 1999; Seiner et al., 2014). For non-compound twins either K_1, ν_2 must be rational (reflection twin or twin type I) or K_2, ν_1 must be rational (rotation twin or twin type II) (Jaswon and Dove, 1960). If K_1 is rational, it may be regarded as a mirror plane which reflects the structure of the twin into that of the parent crystal. If ν_1 is rational, it may be regarded as an axis about which a rotation of 180° transforms the structure of the twin into that of the matrix crystal. Twinning of either type may be produced by mechanical means. On the macroscopic scale, the deformation effectively consists of homogeneous simple shear displacements parallel to the plane K_1, in the direction ν_1 (Jaswon and Dove, 1960; Sozinov et al., 2011).

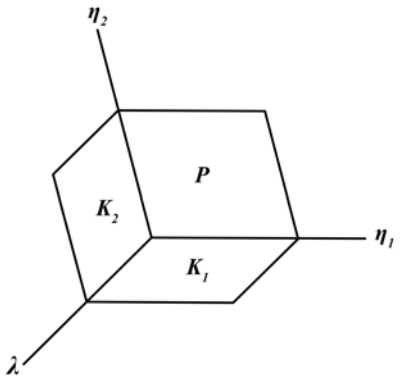

Figure 2.2: Relation between planes K_1, K_1, P and directions ν_1, ν_2,λ, an illustration of twinning elements proposed by Jaswon and Dove (1960)

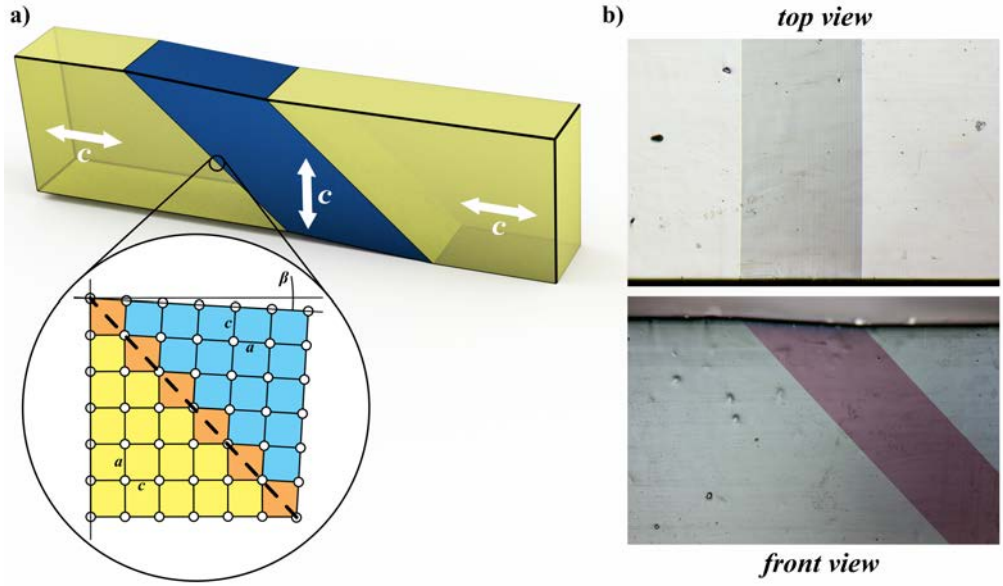

Figure 2.3: (a) Schematically depicted MSM element in the twinned state and 2D representation of the twin boundary in tetragonal approximation of crystal lattice. (b) Aligned micrographs of the MSM element from two sides.

Figure 2.3a illustrates an example representation of the crystallographic structure of a sample with two twin boundaries (TBs) in tetragonal notation. The most significant change of the sample shape is observed when TB intersects with the surface parallel to {100}. The difference in spatial orientation of twin variants divided by TB is represented by the angle β in Figure 2.3a. This angle can be found from the lattice parameters of the crystal:

$$\beta = \frac{\pi}{2} - 2 \cdot \arctan\left(\frac{c}{a}\right) \tag{2.1}$$

For $Ni_{50}Mn_{28.5}Ga_{21.5}$ 10M martensite lattice parameters in tetragonal approximation are a =

b = 0.596 and c = 0.558 (nm), which gives the value of β = 3.77° (Sozinov et al., 2011). The presence of this surface inclination allows optical observation of the twinned structure in MSM samples (see "top view" in Figure 2.3b). Twin variants can also be recognised using polarised light contrast (see "front view" in Figure 2.3b).

2.3 Magnetic shape memory effect

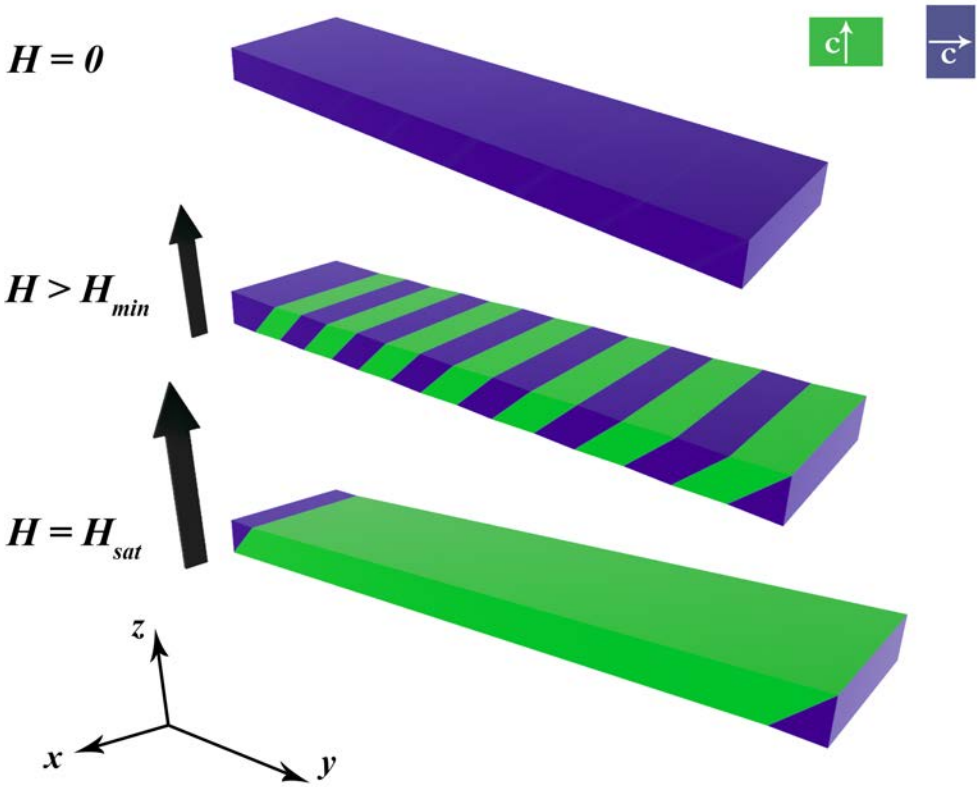

Figure 2.4: A schematic illustration of the magnetic shape memory effect. Green color marks twin variants with easy magnetisation c-axis aligned with the applied magnetic field, blue - with easy c-axis oriented perpendicularly to the field.

Magnetic shape memory effect was first demonstrated by Ullakko et al. (1996). The existence of ferromagnetic twinned martensite microstructure is a precondition for the existence of the magnetic field induced strain (Ullakko et al., 1996; Straka et al., 2011). The mechanism behind the MSM effect is the magnetically induced reorientation (MIR) of the crystal lattice by twin boundary (TB) motion (Ullakko et al., 1996; Likhachev and Ullakko, 2000; Aaltio et al., 2016). The maximum value of MFIS is mainly determined by the crystallographic lattice parameters. For the 10M martensite typical MFIS value at RT lays in the range of 6 – 6.3 %. However, the giant MFIS of nearly 12 % in NM martensite at temperatures above 310 K has been recently

reported by Sozinov et al. (2017). It is almost two orders greater than the strains that can be achieved with piezoelectric and magnetostrictive materials: 0.4 % for piezoceramics and up to 0.17 % for Terfenol-D (Mayergoyz, 1999; Wilson et al., 2007; Murakami et al., 2018).

Such material must be ferromagnetic in martensitic phase with a high magnetic anisotropy when compared to the energy necessary to move the twin boundaries in order to exhibit the MSM effect. In other words, the magnetic stress produced by the material under the exposure to a magnetic field should be higher than the twinning stress. This is expressed by the following equation proposed by Ullakko (1996):

$$U_k > E_{tw} + W + E_0, \tag{2.2}$$

where U_k is the magnetic anisotropy energy, $E_t w$ is the energy required for TB motion, W – work performed by actuation and E_0 expresses all other energy terms. A quantitative model of the MSM effect can be found in (Likhachev and Ullakko, 2000). Schematic illustration of the MSM effect is depicted in Figure 2.4. Magnetic field $\boldsymbol{H}$ is applied perpendicularly to the initial orientation of the easy magnetization c-axis of the MSM element. When the field reaches the minimum value (which depends on material composition, quality of SC and preallocated TB type), TBs starts to propagate and twin variants with easy c-axis aligned with the field grow at the expense of other variants with different orientation. The maximum strain is achieved when magnetic field saturates the material. For 10M martensite the saturation magnetic field is $\mu_0 H \sim 0.6$ T (Dunand and Müllner, 2011; Aaltio et al., 2016).

2.4 Applications

Ni-Mn-Ga material possesses a variety of properties that defines its application fields:

- The actuation of the material can be controlled via self-sensing, twin structure reorientation will cause the change of the magnetic permeability of the element (Hubert et al., 2012)
- TBs type II can develop large speed in saturation magnetic field (Smith et al., 2014; Saren et al., 2016a)
- Due to the spatial reorientation of the martensitic twins via TBs motion, the stroke produced by an MSM element is retained after the mechanical stress or magnetic field are removed
- The TBs movement can dissipate energy, enabling the damping applications (Nilsén et al., 2018)
- Locally applied inhomogeneous magnetic field can create the shrinkage that can carry gasses or liquids if the element is embodied into the elastomer (Ullakko et al., 2012)
- Due to the significant anisotropy between the hard and easy axes of magnetization, MSM material can be used in energy harvesting applications (Saren et al., 2015)

MSM materials should undergo the martensitic phase transformation above ambient temperature in order to be used in real life applications. Moreover, there are environments that require operation at higher temperature, and recent research is showing that MSM alloys are promising candidates for such applications (Pérez-Checa et al., 2017, 2019).

2.5 Microdevices based on Ni-Mn-Ga

The MSM alloys were previously used in micro- and nanoactuators as shape memory material: Ni-Mn-Ga beams exhibited reversible thermal and thermomagnetic shape memory effect down to 100 nm (Kohl et al., 2014a; Kalimullina et al., 2014). The operating principle there is based on the austenite-martensite phase transformation induced by heating and/or by magnetic field application. However, to obtain the true advantage of the MSM effect, especially the fast and large actuation simultaneously, MIR must be employed.

Extensive review on MSM microactuation can be found in (Kohl et al., 2014b). Single crystalline MSMA foils were prepared by cutting thin plates from a bulk single crystal. Subsequent thinning to the desired thickness was performed by a series of mechanical grinding and electrochemical polishing (Heczko et al., 2008). Minimum foil thicknesses have been prepared down to about 50 µm. The material properties that were obtained fulfill the requirements for MIR and thus open up the opportunity to develop miniature MSM actuators. However, technological challenges here are related to the minimization of surface defects created during foil fabrication. Sputtering is another appealing method used to create MSM microstructures. The resulting film structure depends on various parameters including substrate, deposition temperature, sputtering power, and annealing conditions (Kohl et al., 2014a,b). However, there is no published research on successful fabrication of the MSM microdevice that would be operated at RT in martensitic phase by a magnetic field application.

3 Objectives of the study and motivation

As follows from the previous chapter the field of MSM microdevices is weekly studied and there are only few publications on a magnetic field actuation of the Ni-Mn-Ga material at microscale. This motivated the Author to accept challenges and fill the gap in MSM research field by performing the following objectives.

Defining the size limits of the magnetic shape memory effect existence

The first objective of the Thesis was to define whether Ni-Mn-Ga alloy preserves its bulk properties when the size of the MSM element is reduced down to microscale. This involved fabrication of MSM foils that were thinned down to 1 μm. However, the existing mechanical techniques allowed thinning of the foil only down to 50 μm as reported by Heczko et al. (2008). Thus, the Author developed a custom electro-chemical etching procedure that allowed for stress-less polishing of the foil edges even below the required thickness of 1 μm. **Publication I** reports on the successful use of such technique. The reported results indicated that micrometer-scale sized Ni-Mn-Ga devices fabricated from a bulk can be actuated by magnetic field. These findings allowed the Author to proceed to the next objective of the present study.

Microstructure prototyping and basic characterization

After successful verification of the possibility of MIR of crystal lattice in Ni-Mn-Ga on the microscale, a natural step was to create a simple prototype of the MSM microdevice. **Publications II** and **III** utilize FIB milling technology to create a micropillar by simultaneously decreasing 2 dimensions of the element. The micropillar remains attached to the bulky specimen allowing for relatively easy handling of such microstructure. The previously developed electro-chemical etching technique was further improved by the Author. The removal of about 2 μm of ion-beam-damaged surface layer enabled magnetic field actuation in pillars. The results demonstrated the feasibility of manufacturing of micrometer-sized magnetic shape memory actuators using focused ion beam technique.

Actuation speed characterization and comparison to the bulk material

According to recent findings, Ni-Mn-Ga demonstrates high actuation accelerations and velocities (Saren et al., 2016a; Saren and Ullakko, 2017). The next objective of this work was to investigate if MSM microdevice does inherit these unique properties of the bulk material. **Publication IV** documents the existence of both type I and type II TBs in MSM material at the microscale. Properties of these twinning interfaces were studied by the magnetic pulse actuation method developed by Saren et al. (2016a). Based on the experimental and modelled results, type I and type II TB were differentiated. The actuation acceleration of micropillars was reported to be approximately an order of magnitude larger than in bulk samples, demonstrating a well-pronounced scaling effect connected to the decrease of cross-section in actuated MSM crystals and therefore the reduction of moving mass. The complete magnetically induced reorientation of the micropillar was obtained in about 5 μs by type II twin boundary motion. The results suggest the possibility of fabricating MSM-based microdevices with working frequencies of 100 kHz.

4 Methods

4.1 Sample imaging

4.1.1 Optical microscopy

Optical microscopy studies presented in the Thesis were performed by the Author. The Author used multiple microscopes equipped with different optics configuration to control the state of the samples and to analyse their behaviour under exposure to magnetic fields. A Meiji Techno "EMZ-5TR + MA502 + PKL-1 SCS" stereo microscope was used to control manual mechanical force application to the micropillars. It was also used for samples observation while gluing and cleaning processes. A Meiji Techno MT7000 trinocular metallurgical microscope system configured with polarised light contrast lenses was used to reveal the twinned structure in the studied Ni-Mn-Ga single crystalline samples. High-quality images of the micropillars and high-speed video footages of the fast actuation of micropillars were made using a customised configuration of Zeiss Axio Scope.A1 microscope system.

4.1.2 Advanced imaging and twinning stress measurements

Atomic force microscopy (AFM) and magnetic force microscopy (MFM) studies were done by A. Saren using a ParkSystems XE 7 AFM system. A high-quality scanning electron microscope (SEM) imaging of the micropillars was mostly performed by L. Klimša, an operator of a FIB-SEM TESCAN FERA3 GM instrument. A Hysitron PI 85 SEM PicoIndenter and a FEI Quanta 3D FEG Dual Beam SEM were operated by J. Maňák, who performed the twinning stress (TS) measurements for the micropillar samples.

4.2 Sample preparation

Ni-Mn-Ga single crystalline (SC) samples used in **Publications I–IV** were cut from oriented SC bars grown in Adaptamat Ltd. by modified Bridgman–Stockbarger method. This method employs the crystallisation of the melt starting from the half-way molten oriented SC seed by moving the crucible through the high temperature gradient zone inside the furnace. Although the Author was not involved in production of single crystals used in this Thesis, he participated in the assembly of the crystal growth furnace and refined the crystal growing process at LUT Material Physics Laboratory, located in Savonlinna, Finland. The study of the properties of the alloyed Ni-Mn-Ga single crystals which were fabricated by the Author can be found in (Pérez-Checa et al., 2019).

4.2.1 Mechanical treatment

All specimens were cut to the desired shape using a precision wire saw (Princeton Scientific Corp., WS-22) equipped with WSG-02 goniometer for precise orientation of the crystal. Cutting wire with the diameter of 40 µm and boron carbide (B_4C) 1:2 slurry mixture with 60% glycerol were used for almost stress-less cutting of the samples. Mechanical polishing of the faces was performed using MTI Precision Auto Lapping/Polishing Machine EQ-Unipol-1202 and by gradually decreasing the abrasive paper particle size from 50 to 1 µm.

4.2.2 Electro-chemical etching

The electrolyte mixture of 1 part of 60% HNO_3 and 3 parts of denatured ethanol was used for all electrochemical etching procedures. A custom electropolishing technique was developed by the Author with the aim to provide controlled material removal while preserving the shape features of the samples surfaces. Electrolyte solution was poured into the externally cooled beaker and continuously mixed with the magnetic chemical stirrer. Pulse width modulated (PWM) voltage was applied between the sample holder (anode) and acid-resistant stainless steel spiral (cathode) immersed into the electrolyte solution. This allowed to wash the sample by constant flux of the electropolishing liquid and remove etching products from its surface. Control over the voltage, frequency and duty cycle allowed to adjust the regime of the etching. The electropolishing regime that removes the surface stresses but preserves the edges of shape features from smoothing is the major achievement of the developed method.

4.2.3 Preparation of MSM foils thinned down to 1 micron

The precision wire saw was used to cut specimens with a shape of 90° disk sector with thickness of 150 ± 20 μm, from a $Ni_{49.5}Mn_{28}Ga_{22.5}$ oriented single crystalline bar of 20 mm in diameter. Austenite transformation of that alloy occurs at 303 K, and the MFIS in the 5M martensite phase is approximately 6% at RT. First, the specimens were electropolished at 273 K in an electrolyte solution of 3 parts of 60% HNO_3 mixed with 1 part of ethanol at a constant voltage of 20V during 20 seconds. Then, the custom electropolishing technique was used to make a thinned edge. The specimen was glued with a conductive glue onto an anode, and a cathode (with the shape of a rod of 1.6 mm in diameter) was placed $\sim$ 1 mm above the sample surface near the edge. The electrolyte flux created by a magnetic stirrer was washing the open surface of the specimen while a PWM voltage was applied between the anode and the cathode. The voltage function had a shape of square pulses of 12 V amplitude and 50% duty cycle at 60 Hz. As a result, the foil retained its initial dimensions, and a part of it, located under the cathode, was thinned from the top side while the bottom side remained flat.

4.2.4 FIB milling of the micropillars samples

Previous studies of MSM micropillars fabricated by FIB milling showed that the mechanical stress required for the twin variant reorientation is significantly higher than the magnetic stress that could be produced by the material (Dunand and Müllner, 2011; Aaltio et al., 2016; Reinhold et al., 2009). One exception is the work by Jenkins et al. (2008), who reported the rearrangement of twin variants in a magnetic field, which was, however, irreversible. Two major reasons for high twinning stress were proposed: surface damage (by Ga^+ ion implantation) and size effect (Dunand and Müllner, 2011; Reinhold et al., 2009). Because the latter was shown to be insignificant down to 1 µm (Musiienko et al., 2017), the surface damage stress induced by ion beam milling should mainly affect the MIR in micrometre-sized pillars, similarly to the bulk material with surface stresses introduced by various methods (Chmielus et al., 2011; Ullakko et al., 2015).

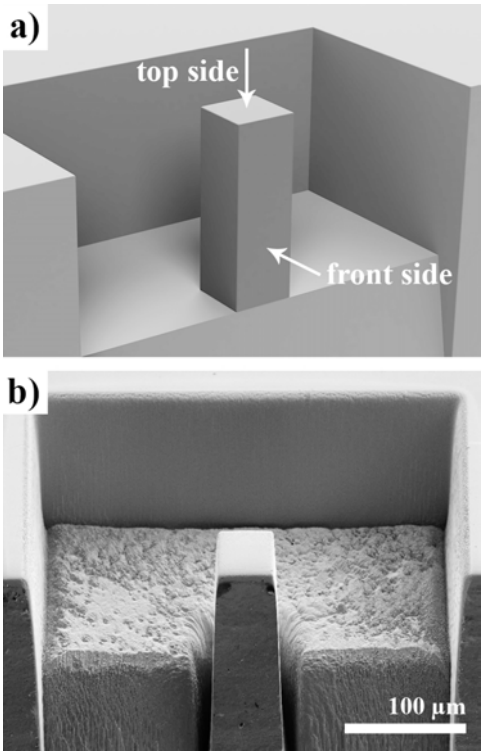

Figure 4.1: (a) Schematic view of Ni-Mn-Ga single-crystalline micropillar and (b) top-front view captured by SE detector in SEM after FIB milling procedure. In (a), the top and front sides of the pillar are marked with arrows.

Three cuboid samples ($6.5\times2.5\times1$ mm^3) were cut from a $Ni_{50}Mn_{28.5}Ga_{21.5}$ single crystal grown in Adaptamat Ltd. using a precision wire saw (Princeton Scientific Corp., WS-22) and then mechanically polished. The chosen single crystal exhibited five-layered modulated martensite structure at room temperature. Martensite transformation and Curie temperatures of the crystal are $T_M = 321$ K, $T_A = 327$ K and $T_C = 371$ K, and maximum possible compressive MFIS derived from the lattice parameters is $1 - c/a = 6\%$. Prior to machining, the specimens were

electropolished and reoriented to the single-variant state by the application of a magnetic field of 1.4 T, which is higher than the saturation field (Dunand and Müllner, 2011). Figure 4.1a depicts a schematic drawing of the desired micropillar. The FIB milling was performed using fully integrated Xe plasma source FIB using scanning electron microscope (FIB-SEM) TESCAN FERA3 GM. Electron-cyclotron-resonance-generated Xe plasma over Ga liquid metal ion source was chosen because of the significant reduction in the depth of ion implantation, thinner damaged layer and an order of magnitude higher milling speed (Ingram and Armour, 1982; Giannuzzi and Smith, 2011; Hrnčíř et al., 2012; Kelley et al., 2013; Burnett et al., 2016). The process was monitored by secondary electrons (SE) imaging (Everhart-Thornley SE detector) at 5 kV / 500 pA for SEM and 30 kV / 10 nA for FIB-generated SE. Rough 100 µm deep milling at 30 kV / 300 nA was performed first. The example of rough milling of the micropillar is presented as consequent snapshots in Figure 4.2. It was followed by a more precise pillar polishing at 30 kV / 100 nA, which gave the final shape to the pillar (see Figure 4.1b). Front side of the pillar was not directly exposed to the plasma beam intentionally. The micropillar had the shape of a truncated pyramid, with a height of 108 µm and rectangular parallel bases with sizes of approximately 50×50 µm (bottom) and 48×43 µm (top). The deviation in the size is due to the non-Gaussian shaped FIB with significant beam tails.

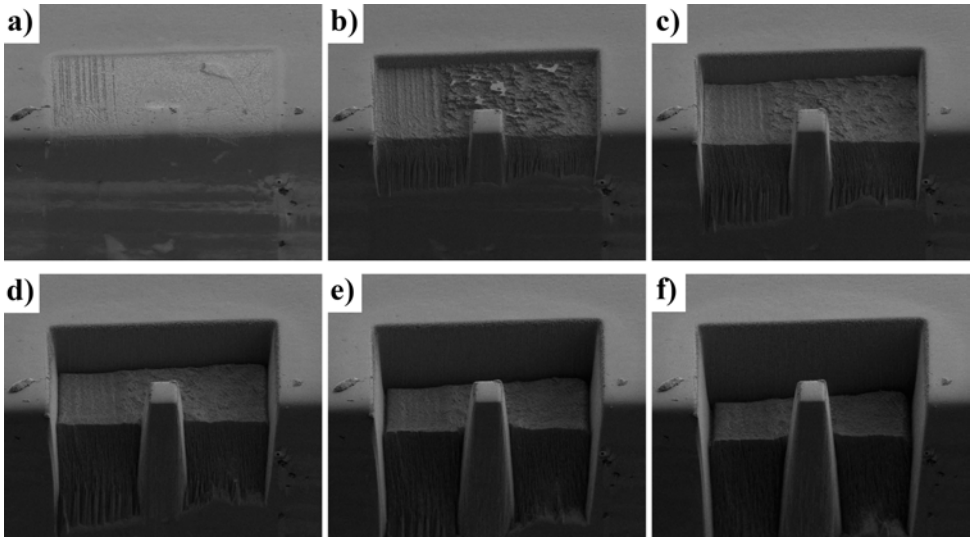

Figure 4.2: Consequent SEM images of the rough FIB milling process.

4.3 Magnetic actuation

Two magnetic actuation stages were developed to study MIR in Ni-Mn-Ga single crystalline foils and micropillars.

4.3.1 Rotating permanent magnet stage

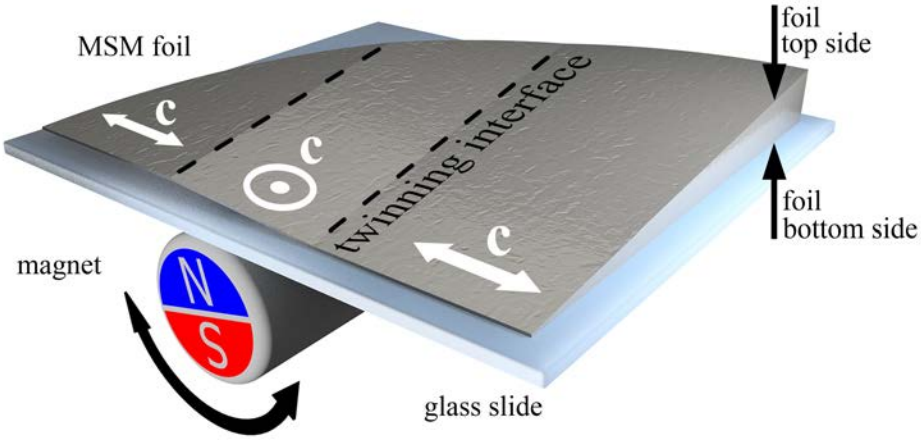

Figure 4.3: Schematic view of the rotating permanent magnet set-up used in **Publication I**. White arrows indicate the direction of the easy c-axis in the twin variants.

Rotating permanent magnet stage is schematically presented in the Figure 4.3. The idea behind such stage is to create an inhomogeneous magnetic field inside the Ni-Mn-Ga material. This actuation method is used in MSM micro-pumps to create the shrinkage that will carry the liquid or gas from the inlet to the outlet (Ullakko et al., 2012). In the case of the Ni-Mn-Ga foils multiple twin boundaries were formed and propagated through the foil, as shown in Figure 4.3.

4.3.2 Electric magnet set-up

The magnetic actuation apparatus used in Publications II–IV is shown in Figure 4.4(a). It consists of rotatable sample holder and custom built electromagnet. Figure 4.4(b) shows the magnetic field distribution within the air-gap calculated using Finite Element Method Magnetics package (Meeker, 2016). The setup was designed for the direct observation of the pillar response to the applied magnetic field in the polarised light microscope.

The electromagnet was capable of creating magnetic fields up to $\mu_0 H = 0.65$ T, which is about the saturation field of the Ni-Mn-Ga SC (Dunand and Müllner, 2011), within 6 mm long cylindrical air-gap between the concentration poles of 8 mm in diameter. The field magnitude was controlled by the PID controller developed in the NI LabView software. It is capable

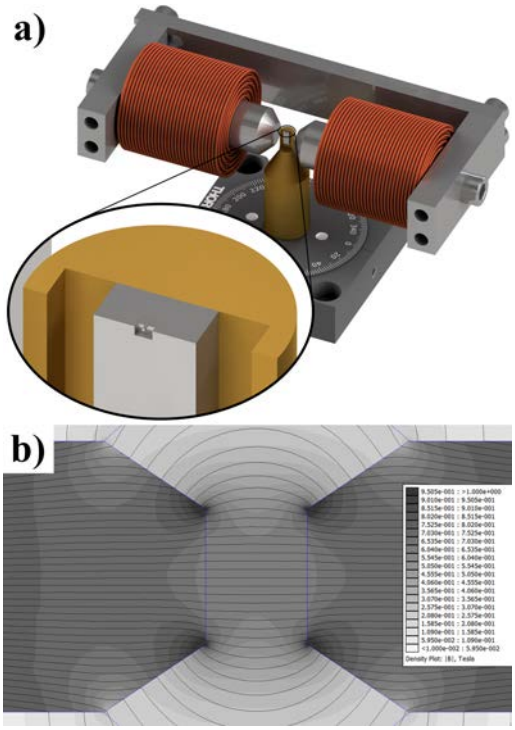

Figure 4.4: (a) Schematic view of the in-house built rotatable sample holder setup equipped with an electromagnet. (b) Magnetic field distribution within the air-gap calculated in Finite Element Method Magnetics package (Meeker, 2016)

of maintaining the highest field during 1 minute before the coils are overheated and require cooling. The control software was paired with the fast camera and magnetic field sweep option was successfully used in Publication III.

4.4 High-speed characterisation

For the fast actuation of the micropillars we used a pulsed magnetic field set-up that was initially developed in Saren et al. (2016b) for bulk, mm-sized MSM samples. Two coaxial coils connected in series (Helmholtz configuration), were used to generate the magnetic field. Each coil has a diameter of 9.1 mm and consists of 20 turns of an insulated copper wire of 0.2 mm in diameter, with a distance between coils of 5.2 mm (see Figure 4.5b). The coils' frame has an axial hole and a few openings between the coils to allow for the positioning of the sample holder and observation the top and front sides of the micropillar. A Polytec OFV-5000, OFV-534 Laser Doppler Vibrometer (LDV), equipped with an additional lens that reduced the spot size down to $\sim$ 1.5 µm, was used to measure the actuation velocity and displacement of the top side of the pillar. The micropillar's shape change during actuation was monitored from the front side by a Photron FASTCAM SA-Z connected to a microscope (Zeiss Axio Scope.A1). The construction of the sample holder and the system's microscope mount allowed for the 90° rotation of the

Helmholtz coil around the sample, providing the possibility for magnetic field application along and perpendicular to the micropillar. Figure 4.5b shows the front view of a schematic cross-section of the micropillar inside the coil during the elongation measurement. The central area of the figure (pictured in the white elliptical frame) is magnified to make the micropillar visible against the Helmholtz coil in the background. Figure 4.5c shows a representative snapshot taken by the built-in LDV camera after the laser beam was focused on the top side of the pillar. To achieve high-speed camera imaging, the micropillar was illuminated by a CoolLED pE-4000 light source through the microscope's reflected light pathway. Magnetic field strength in the place of the micropillar was calculated from the measured Helmholtz coil current. The pulse circuit was configured to provide a square-like current pulse with a length of $\sim$ 60 µs and an amplitude of 230 ± 15 A which corresponds to magnetic field of 0.85 ± 0.05 T. Front edge of the pulse was reaching the saturation magnetic field of $\sim$ 0.6 T in $\sim$ 2 µs.

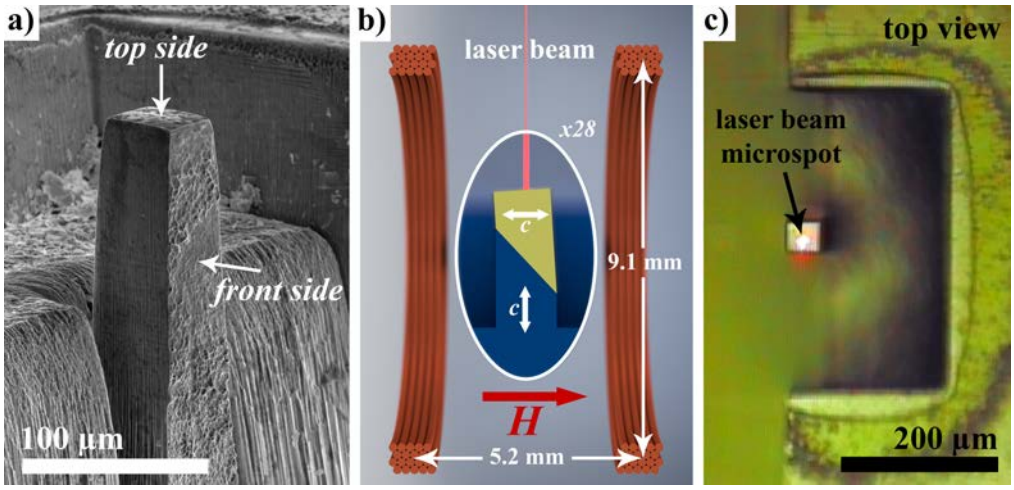

Figure 4.5: (a) SEM image of a FIB-milled MSM micropillar after electro-polishing. (b) Schematic cross-sectional front view of the micropillar inside the Helmholtz coil during elongation measurement. The central area of (b) (pictured within the white elliptical frame) is magnified 28 times. The directions of the easy c-axis in different twin variants are marked by the white arrows, and the direction of the magnetic field $\boldsymbol{H}$ is marked by the red arrow. (c) Top view photograph of the micropillar taken with a built-in LDV camera prior to actuation. The LDV laser beam is focused on the top side of the pillar.

The micropillar shape change during actuation was monitored from the front side by a Photron FASTCAM SA-Z connected to a microscope (Zeiss Axio Scope.A1). To achieve high-speed camera imaging, the micropillar was illuminated by a CoolLED pE-4000 light source through the microscope reflected light pathway. All pulsed magnetic field actuation experiments were performed by A. Saren together with the Author.

4.5 Mechanical testing

To measure the twinning stress (TS) required to move TBs of different types we utilised a measurement technique that is being developed by Dr. Marek Vronka and Mr. Jan Maňák at the Institute of Physics of the Czech Academy of Sciences, Prague, Czech Republic. A custom-made boron-doped diamond punch with a diameter of 20 µm at its flat end was used to push the micropillar from the top side. Prior to each measurement, the micropillar was fully elongated in a magnetic field.

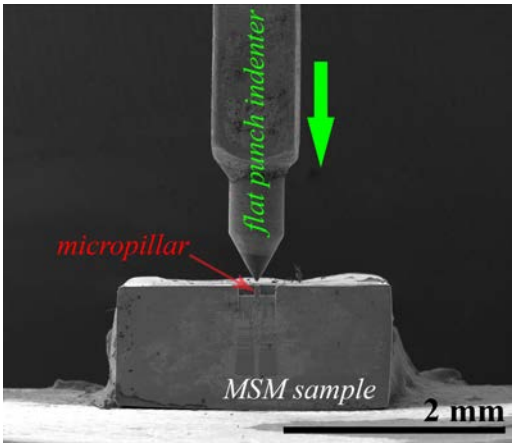

Figure 4.6: Flat punch indenter in a close approach to the micropillar sample, that is glued to SEM sample holder by a conductive silver paint.

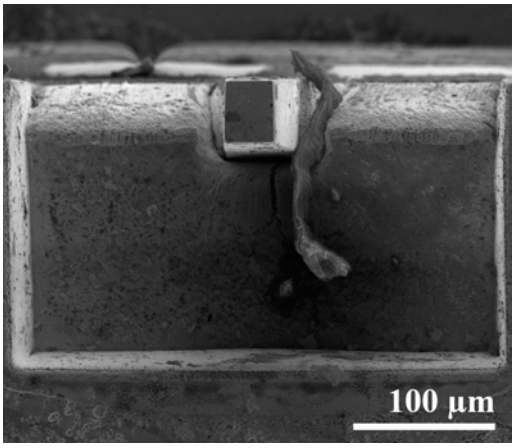

Figure 4.7: Top view SEM image of the micropillar that was used to measure cross-sectional area values for the micropillar.

The process was monitored by scanning electron microscope (SEM) to ensure that only a single TB was being moved. Compression of the micropillar was performed using a Hysitron PI 85 SEM PicoIndenter inside a FEI Quanta 3D FEG Dual Beam SEM. The errors in force and

displacement measurement were 400 nN and 1 nm, respectively. An Everhart Thornley detector was used to capture electron micrographs of the micropillar during the compression process. The process was monitored by scanning electron microscope (SEM) to ensure that only a single TB was being moved. Force and punch displacement data was recorded synchronously with continuous SEM scan captured by ETD.

The construction of the indentation machine allowed 3-axial alignment of the micropillar sample using linear translation piezo-motors. Angular alignments were performed manually with the aid of stereo-microscope prior to installation of the indentation device into the SEM vacuum chamber. Figure 4.6 shows the SEM image of the indenter and micropillar sample after the spatial alignment of the flat punch. Top view SEM image (see Figure 4.7) was made to define cross-sectional area values of the micropillar in fully contracted state. These data were used to derive TS values from the force-displacement measurements. Twinning stress was defined as force divided by the cross-sectional area of contracted micropillar in the central point of the twin boundary. High-resolution SEM images of the front side of the micropillar prior to and after the compression test are shown in Figure 4.8. Approximate TB positions (defined from the tilt angle of the pillar edges) are denoted by dashed lines.

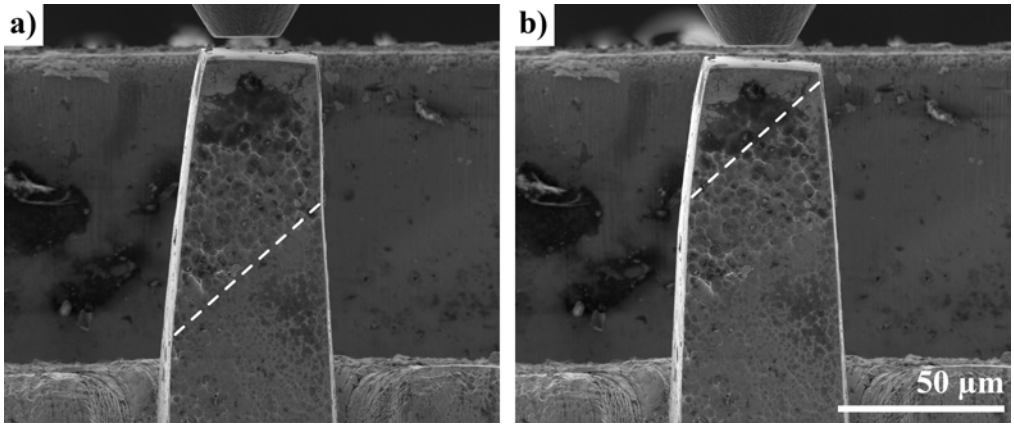

Figure 4.8: SEM images of the micropillar before (a) and after (b) the compression test. Dashed lines indicate approximate position of the twin boundary defined from the tilt angle of the pillar edges. Both images are presented in the same scale.

4.6 Variable-mass actuation model for MSM micropillars

The model developed earlier for single TB motion in (Saren and Ullakko (2017)) for bulk, mm-sized samples was adapted by A. Saren for the micropillars. For simplicity, it is assumed that the micropillar had a cuboid shape with a constant cross-section of 40×43 μm^2. It is an average cross-section of the active part of the micropillar where the TBs are movable. The crystal tetragonality used in the model is $c/a = 0.941$, according to the measured transformation strain of 0.059 of the alloy.

Figure 4.9 schematically describes the twin variant structure in the micropillar during application of a magnetic field in the perpendicular direction. The applied field causes elongation of the micropillar because the favourable, left variant has its short easy c-axis aligned with the field and grows at the expense of the right variant. During elongation, the TB moves to the right at the velocity $\boldsymbol{V_{TB}}$, and the left edge of the pillar moves to the left at the elongation velocity $\boldsymbol{V_E}$. The driving force $\boldsymbol{F}$ is applied to the moving variant and is equal to the difference between the magnetic driving force and resistance force. This resultant force causes the left variant motion and pillar's elongation.

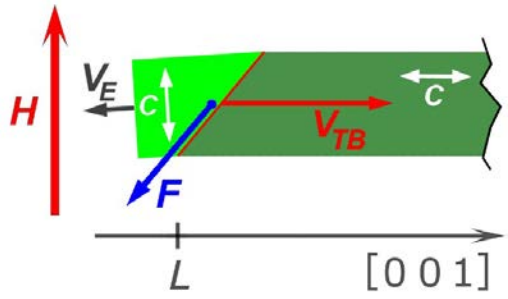

Figure 4.9: Schematic representation of the micropillar twin variant structure in elongation mode (corresponds to the front view of the micropillar in the article text). White arrows show the easy c-axis orientation inside the twin variants. The TB position measured along the [001] direction in the pillar's base is denoted by L. Vectors $\boldsymbol{H}$, $\boldsymbol{V_{TB}}$, $\boldsymbol{V_E}$ and $\boldsymbol{F}$ denote the applied magnetic field direction, TB velocity, elongation velocity and the driving force acting on the moving variant, respectively. (Courtesy of Dr. A. Saren, LUT University, published with permission.)

Analogously to the case presented in (Saren and Ullakko (2017)), here the mass of the moving variant continuously increases. This leads to derivation of a similar dynamic equation that describes the motion of the moving variant in terms of the TB position, L, change with time t:

$$\left(\frac{dL}{dt}\right)^2 + \left[\frac{m_0}{\rho A_0} + (L - L_0)\right]\frac{d^2L}{dt^2} = \frac{k_0'}{\rho}\cos\alpha'[\sigma_{mag} - \sigma_{res}], \tag{4.1}$$

where A_0 is the cross-section of the right part of the pillar, m_0 - the initial mass of the moving variant, ρ - volumetric mass density of the alloy (8000 kg/m^3), L_0 - the initial TB position, k_0' and α' are parameters defined by the lattice tetragonality ratio c/a. In the present case, the calculated values of the lattice related parameters are as follows: $k_0' = 11.28$ and $\alpha' = 46.74°$.

The stresses σ_{mag} and σ_{res} in the right part of Eq.4.1 describe magnetic field-induced stress and resistance stress, correspondingly. The magnetic field-induced stress depends on the applied

field, and thus it is time-dependent for a pulsed magnetic field. The resistance stress can be represented as a quasi-static twinning stress value plus a second term, which is dependent on TB velocity. The details on representation of these stresses can be found in (Saren and Ullakko, 2017).

From Eq.4.1, it follows that at a limited driving stress the TB velocity will saturate reaching a maximum value of

$$V_{TB}^{max} = \left(\frac{dL}{dt}\right)_{max} = \sqrt{\frac{k_0'}{\rho}\cos\alpha'[\sigma_{mag} - \sigma_{res}]}. \tag{4.2}$$

The velocity saturation indicates a state when the momentum of the moving variant is increasing only because of the growth of its mass. TB motion is modelled by numerical integration of Eq.4.1, using standard numerical solving algorithms for ordinary differential equations found in MATLAB® R2017a software.

5 Results and Discussion

5.1 MSM effect in single crystalline Ni-Mn-Ga foil

In order to reveal whether MSM effect can be utilised in microdevices based on single crystalline Ni-Mn-Ga alloys, we prepared foils thinned towards one edge. The goal of the **Publication I** was to study the possibility of magnetically induced reorientation of the crystal lattice in Ni-Mn-Ga foil samples with the thickness down to 1 µm. This section will reveal and discuss the results of the first step in our research – one dimensional approach.

5.1.1 MIR of thinned Ni-Mn-Ga foil

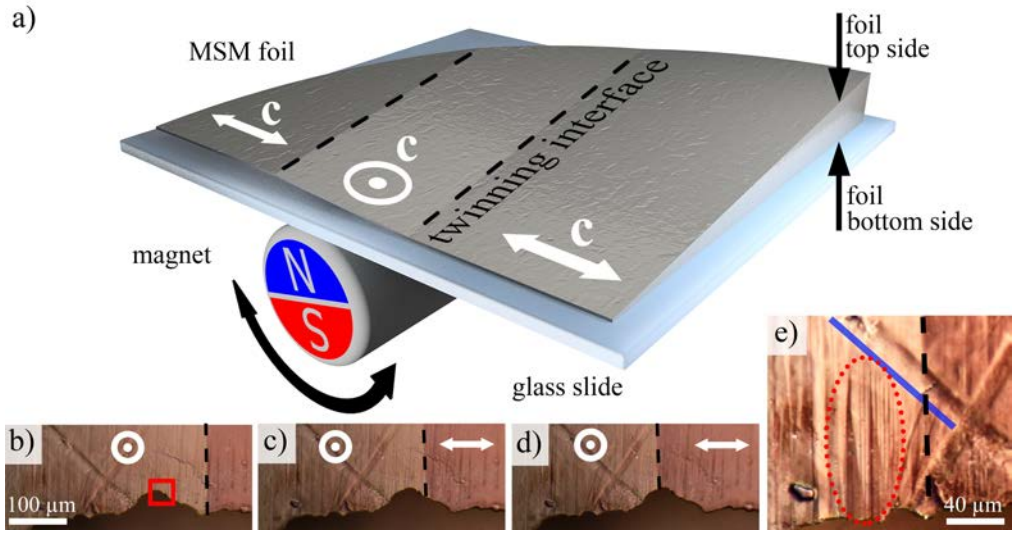

Figure 5.1: (a) Schematic view of the experimental setup used to magnetically induce reorientation of twin variants in the foil sample. (b-e) Optical micrographs of the bottom side of the specimen in polarised light showing subsequent steps of the twinning interface motion through the thinnest edge of the foil caused by rotation of the magnet. The twinning interface is denoted by the dashed line. White arrows indicate the direction of the easy c-axis in the twin variants. Red square highlights the region studied by AFM/MFM. (e) Optical micrograph representing the appearance of multiple variants (see the area highlighted by the red dots) constrained by a surface defect (denoted by the blue line).

A diametrically magnetised cylindrical magnet (⌀6.35 × 25.4 (mm), NdFeB, Grade N42) with a maximal surface field of ~ 0.6 T was used to produce MIR of twin variants in the studied sample, as shown in Figure 5.1a. The optical images (see Fig. 5.1b-d) represent the motion of a twinning interface through the thinnest part of the sample caused by a continuous rotation of the magnet.

The observed MIR of twin variants is possible due to magnetic field distribution in the Ni-Mn-Ga sample created by the diametrically magnetised magnet which was studied by Ullakko et al.

(2012). The foil exhibits 6 ± 1 % transformation strain that was measured from micrographs depicted in Figure 5.1(b-d). Figure 5.1e shows multiple twin variants which appeared and grew in a small region separated from the thicker part of the foil by a surface defect. These twins were constrained by the aforementioned defect at the thicker part of the region with the thickness measured to be 12 ± 2 µm, while they were freely expanded at the ~ 1 µm edge of the foil by the applied magnetic field. The behaviour of the crystal structure in this region indicates that there are no signs of inhibition of MIR related to the small, ~ 1 µm, thickness of the foil.

5.1.2 Magnetic domain structure characterisation

To characterise the shape and magnetic domain (MD) structure of the specimen's thinnest edge, an atomic force microscope (AFM) with magnetic force microscopy (MFM) feature (ParkSystems, XE 7) was used. Initially, the sample was switched to the state with the c-axis perpendicular to the surface of the foil. Roughness of the bottom surface was evaluated by AFM to be in the range of 0.2 µm near the thinnest edge. After that, the bottom side of the sample was glued to the glass slide while exposed to saturating magnetic field. The purpose of the magnetic field was to keep the sample in a single-variant state and to press the sample against the glass surface.

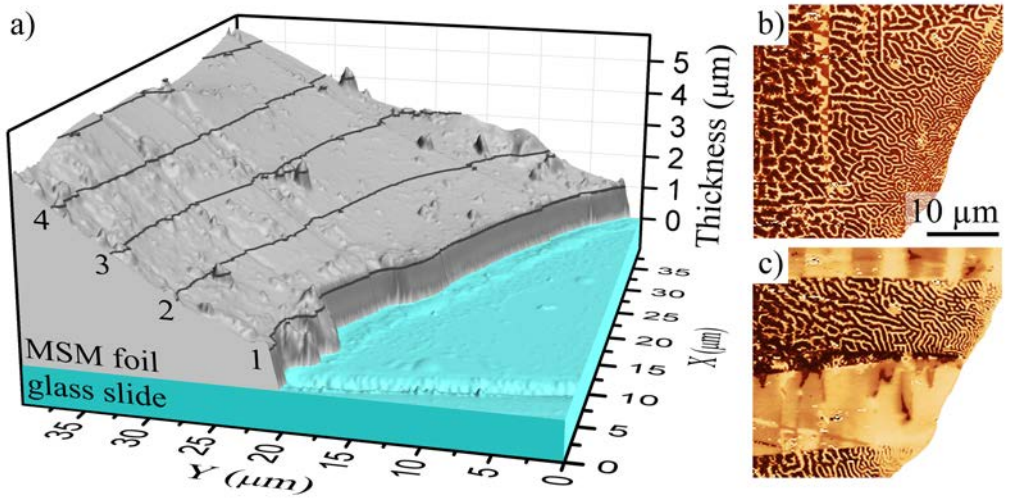

Figure 5.2: (a) AFM topography map of the top side of the thinned edge of the foil (see the chosen region marked in Figure 5.1b). Glass slide surface serves as zero-level of the thickness profile, isolines are shown for each 1 µm of the thickness. Front face of the picture is artificially coloured for the ease of visual perception. (b,c) MFM scans of the same region: (b) single variant state with easy magnetisation axis perpendicular to the plane of the scan; (c) multi-variant state. Magnetic domains are arranged in a characteristic "labyrinth" structure. Their characteristic width decreases with the thickness of the foil from the left to the right.

The 3D view of the AFM scan of the chosen area (see the red rectangle in Figure 5.1b) taken from the top side of the foil is shown in Figure 5.2a. Thickness of the edge of the tapered sample was measured to be 1 µm including the glue layer. After that, the specimen was detached from the glass by dissolving the glue in acetone. As reported by Heczko et al. (2015b), a bulk

Ni-Mn-Ga exhibits a characteristic "labyrinth" MD structure. The MFM scans from the top side of the chosen region in a single- and multi-variant state (Figures 5.2b and 5.2c) show that the studied sample has the same MD structure. This observation proves that the magnetic structure of a bulk material is retained down to the micron scale in the studied Ni-Mn-Ga alloy.

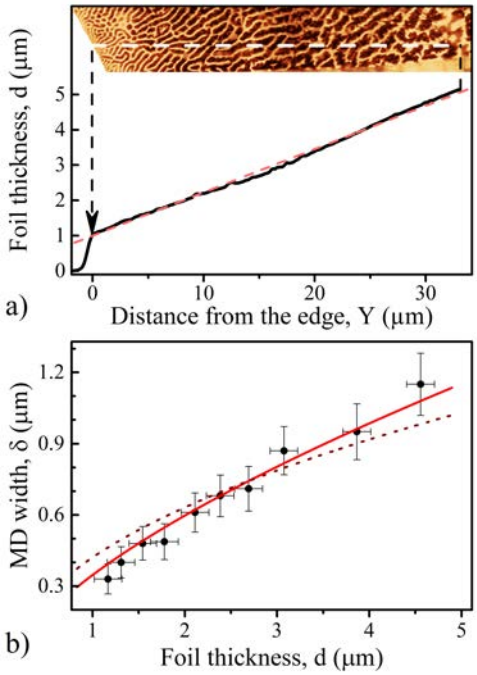

Figure 5.3: (a) MFM image taken from the bottom side of the foil (inset) and corresponding foil thickness profile obtained from the AFM scan (Figure 5.2a). Dashed red line is a linear fit with an intercept value of 1 μm and a slope of 0.12 ± 0.01 μm/μm. (b) Magnetic domain characteristic width, δ, dependence on the thickness of the foil, d. Dashed and solid fitting curves are power functions with the exponents of $1/2$ and $2/3$, correspondingly (see Eq. 5.1).

In order to improve the quality of the magnetic structure image, we made MFM scan from the bottom side of the chosen area, shown in the inset of Figure 5.3a. The thickness profile of the thinnest edge of the foil derived from the AFM scan (Figure 5.2a) is presented in Figure 5.3a. It was characterised to be linear with a slope of 0.12 ± 0.01 μm/μm. The characteristic width of MDs, δ, was calculated from the MFM image and is shown in Figure 5.3b as a function of the foil thickness. Data was fitted by the following power function used for magnetically anisotropic thin films (Hubert and Schäfer, 2008):

$$\delta = \xi_\alpha (d - d_0)^\alpha, \tag{5.1}$$

where d is the film thickness, d_0 – an error of thickness measurement, and ξ_α – a coefficient related to the anisotropy and exchange energies of the material. Theoretical value of the exponent α equals $1/2$ for a thin film and $2/3$ for a thick film in which domain branching occurs (Hubert and Schäfer, 2008). For the presented data, considering $d_0 \leqslant 0.2$ μm, it was found that the value of $2/3$ for α provides better fit (see Figure 5.3b). This indicates that MDs should have a branched micro-structure down to foil thickness of 1 μm. In the presented MFM images, the

branching of the domains is clearly observable starting from the foil thickness of 2.5 µm. We suppose that for smaller thicknesses, branching is not visible due to the limitations of the MFM scan resolution.

5.2 Giant MFIS in Ni-Mn-Ga micropillars

In the previous section we have shown that if one dimension of the Ni-Mn-Ga single crystal is decreased to 1 µm, the MIR is not hindered. Here we will talk about the investigation of a micropillar which was created by decreasing two dimensions of a bulk structure with the aid of the FIB milling technology. Data discussed in the current section was published in **Publication II** and presented in oral form at the 16th International Conference on New Actuators ACTUATOR2018 (**Publication III**).

5.2.1 Ni-Mn-Ga micropillars

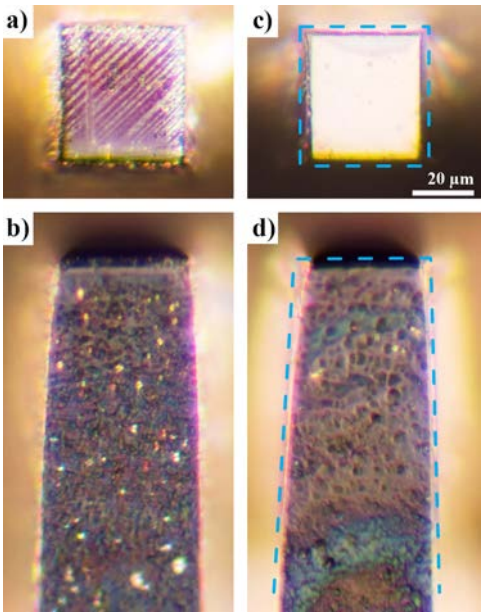

Figure 5.4: (a,b) Ni-Mn-Ga micropillar top and front sides after fabrication and (c, d) after electropolishing captured by optical microscope under polarised light. Two-variant micro-structure visible in (a) is caused by surface stresses induced by the ion beam milling. A single-variant state is observed in (c, d) after the damaged surface layer was removed by electro-chemical etching. The contour of the sample after fabrication from (a, b) is indicated by dashed line in (c, d) for comparison. All micrographs have the same scale.

Optical micrographs of the micropillar in polarised light right after FIB machining are presented in Figure 5.4(a,b). A fine twin structure was observed on the top side (Figure 5.4a) because of the surface stresses induced by ion beam milling to other faces of the micropillar.

According to Burnett et al. (2016), the thickness of a damaged layer should be approximately 100 nm. To provide a controlled smooth removal of the surface deformation layer, the electropolishing technique described in Musiienko et al. (2017) was used. All the electrochemical etching procedures were made in an electrolyte mixture of 1 part of 60% HNO_3 and 3 parts of denatured ethanol kept at 253 K. Pulse width modulated voltage (at 50 Hz) was applied between the sample (anode) and acid-resistant stainless steel spiral (cathode) immersed into the electrolyte solution which was constantly mixed using a magnetic chemical stirrer. All the electropolishing procedures were controlled by voltage modulation. The samples with the micropillars were electropolished gradually in steps of 10 s. After each procedure of the surface removal, the micropillar was tested in the magnetic field of 1.1 T. It was found that after a total duration of 90 s, the micropillars showed a fully reversible MIR of twin variants.

Optical views of the micropillar after electrochemical etching are shown in Figure 5.4(c,d). Comparison of the pictures of the micropillar before and after electropolishing showed that the thickness of the removed surface layer was in the range of $0.5 - 4$ μm, with an average of approximately 2 μm. Because of the specific electric field distribution caused by the complex structure of the sample, the surface layers removed from the edges and the top face of the micropillar were thicker than the ones removed from the micropillar bottom and bulk specimen. Figure 5.5 shows the SEM images of the electropolished micropillar.

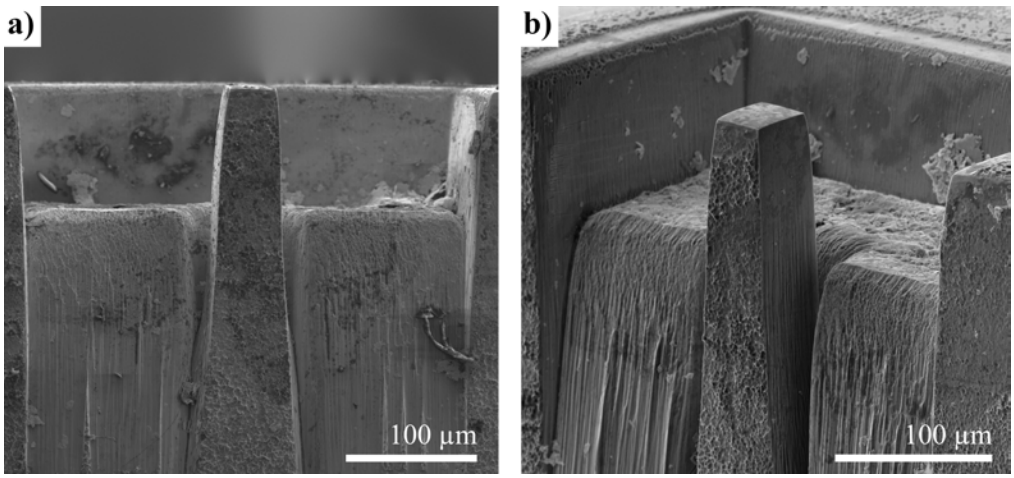

Figure 5.5: SEM images of the micropillar after electrochemical etching: (a) front view and (b) perspective view.

5.2.2 Magnetic actuation of the micropillars

Prior to investigation of MIR in the micropillar, a magnetic field of 1.5 T was applied to the sample along the longest dimension of the micropillar to reorient it to a single-variant state. The sample was glued with a super glue onto the sample holder to ensure that TBs will move only within the micropillar and will not be driven by the MIR of twin variants in the bulk. The sample holder was mounted on a rotatable stage inside the electric magnet (see Figure 4.4) so that the front side of the micropillar was observed by the microscope.

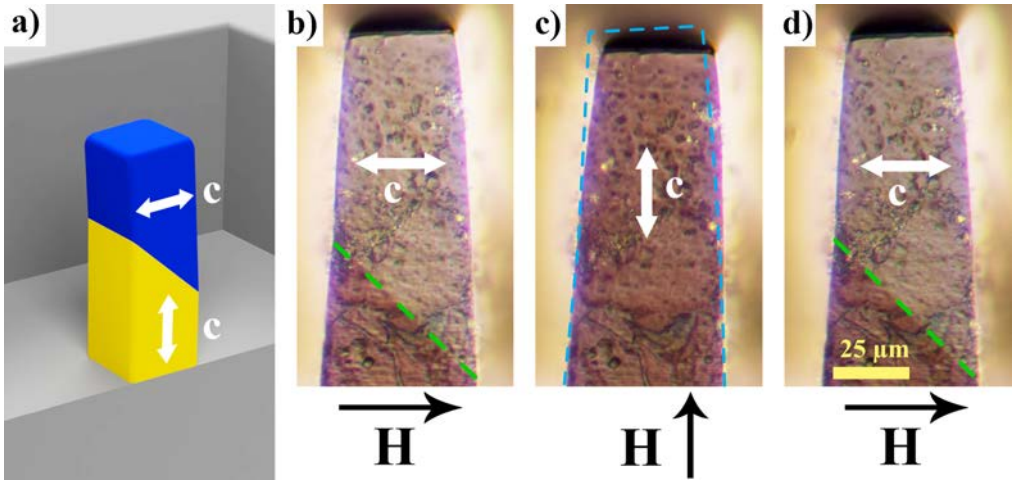

Figure 5.6: (a) Schematic view and (b, c, d) front face optical images demonstrating magnetically induced reorientation of twin variants in Ni-Mn-Ga micropillar. Directions of magnetic field ($\mu_0 H$ = 0.5 T) applied before taking each picture, are denoted by black arrows. Twin variants are distinguished by polarised light contrast. Twin boundaries in (b) and (d) are indicated by green dashed lines. White arrows show the direction of c-axis in the micropillar. Micropillar contour from (b) is denoted by dashed cyan line in (c) for reference. All micrographs have the same scale.

There are two possible TB orientations for the longitudinal micropillar actuation. Figure 5.6a represents the schematic view of the first orientation. MIR of the micropillar was performed by the repeated application of the magnetic field ($\mu_0 H$ = 0.5 T) in two perpendicular directions. Figure 5.6b shows the optical micrograph of the micropillar after the magnetic field was applied perpendicularly to the longest dimension of the micropillar. Then, the field was applied along the micropillar, which resulted in a full MIR (Figure 5.6c). The change in the length of the active part of the micropillar was optically measured to be 6 ± 0.5 %. Figure 5.6d shows that the MIR is fully reversible and repeatable.

To find the lowest external field that causes the TB motion in the micropillar a Photron FASTCAM SA5 model 775K-M2 was mounted onto the microscope. The MIR of the micropillar was recorded at 30,000 frames per second, the footage was temporally synchronised with the magnetic field sweep from the remanent field of 0.02 T up to 0.65 T. Polarised light contrast was used to distinguish the TB position. Figure 5.7 represents the indicative frames of the footage with corresponding values of applied magnetic field. The TB motion occurs in steps, which is explained by the non-uniform field distribution within the sample (Heczko et al., 2015a).

To retrieve the initial state of the micropillar (fully contracted) the sample holder was rotated 90°. During the magnetic field sweep, TB moved through the entire pillar within less than 0.1 ms when the field reached value of 0.12 T.

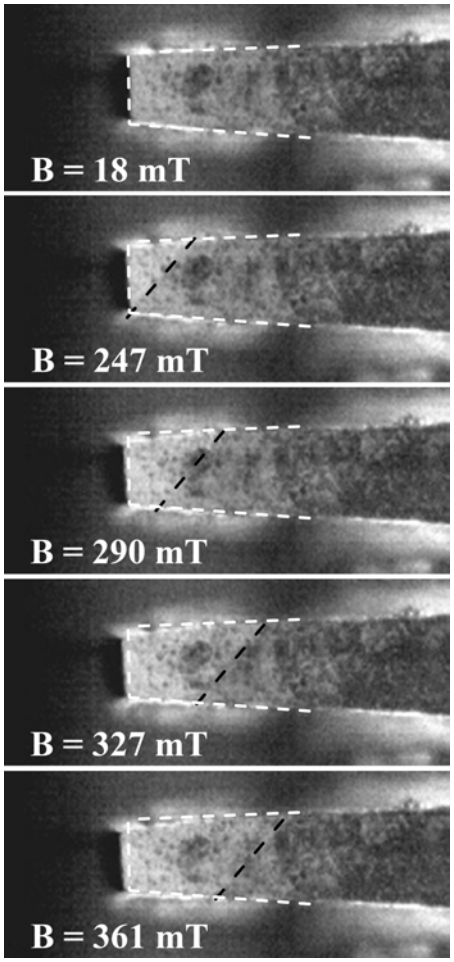

Figure 5.7: Temporally ordered optical micrographs of the MIR of the micropillar during the magnetic field sweep. TB position is denoted by black dashed line for each frame. White dashed line denotes initial micropillar shape on each frame for the reference.

5.2.3 Magnetic domain structure

The second TB orientation variant was induced by repeated magnetic field application in another pair of perpendicular directions (a normal to the front and a normal to the top sides of the pillar). Figure 5.8a shows the schematic view of such TB orientation. Magnetic field microscopy image of the highlighted region of size 40×40 µm^2 in Figure 5.8a is presented in Figure 5.8b. We observed a branched magnetic domain (MD) structure in the martensite variant with the easy magnetisation axis perpendicular to the surface and a 'needle-like' MD structure in the variant with the c-axis lying in the surface plane (Lai et al., 2010). The observed MD structure is inherited from the bulk material (Heczko et al., 2015b). This confirms that magnetic properties of the studied object are similar to those of the bulk.

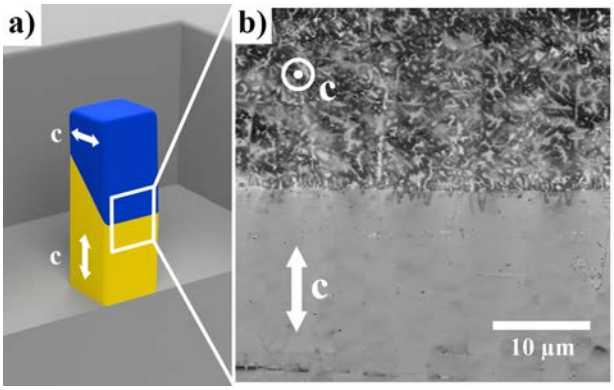

Figure 5.8: (a) Schematic view of the Ni-Mn-Ga micropillar after changing its twinning structure and (b) magnetic force microscopy image of the highlighted region in (a). White arrows show the direction of the easy magnetisation c-axis.

5.3 Ultrafast actuation of Ni-Mn-Ga micropillars

The next step in our research plan was to investigate MSM actuation kinetics at the microscale. We combined experimental and modelling approaches to explore the difference in mobility of type I and type II TBs in micropillars.

5.3.1 Pulsed magnetic field actuation

For the fast actuation of the micropillars we used a pulsed magnetic field set-up that was initially developed by Saren et al. (2016b) for bulk, mm-sized MSM samples. A Polytec OFV-5000, OFV-534 Laser Doppler Vibrometer (LDV), equipped with an additional lens that reduced the spot size down to $\sim$ 1.5 µm, was used to measure the actuation velocity and displacement of the top side of the pillar. The micropillar's shape change during actuation was monitored from the

front side by a Photron FASTCAM SA-Z connected to a microscope (Zeiss Axio Scope.A1). To achieve high-speed camera imaging, the micropillar was illuminated by a CoolLED pE-4000 light source through the microscope's reflected light pathway. Magnetic field strength was calculated from the measured electric current curves. The pulse circuit was configured to provide a square-like magnetic pulse with a length of ~ 60 µs and a magnitude of ~ 0.8 T. The front edge of the pulse was reaching the saturation magnetic field of ~ 0.6 T in ~ 2 µs. The details about the measurement set-up can be found in chapter **4 Methods**.

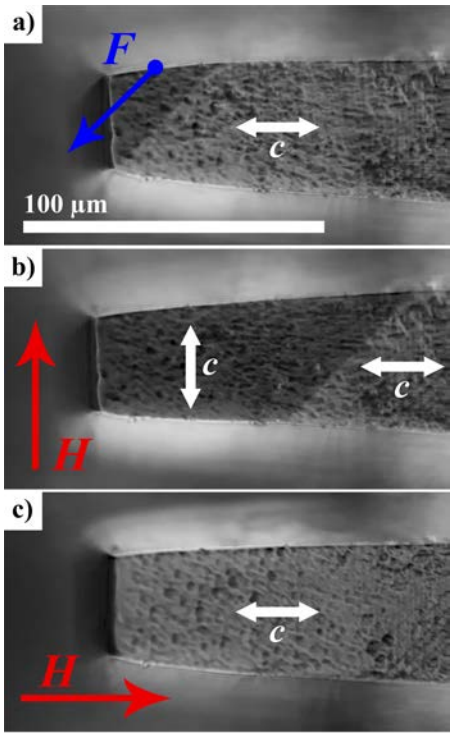

Figure 5.9: Optical micrographs of the front side of a micropillar showing the stages of elongation-contraction measurement. Twin variants are differentiated by the optical contrast in polarised light and the easy c-axis orientations are marked by white arrows. (a) Initial state with purposely introduced type I TB. The direction of the mechanical force ***F*** and application point are marked by the blue arrow and dot, respectively. (b) Elongated state after pulsed magnetic field application perpendicular to the micropillar. (c) Contracted state after a magnetic pulse application along the micropillar.

Prior to the TB kinetics investigation, two samples were glued to the sample holders in a single variant state with the easy c-axis oriented along the micropillar. The same acrylic glue was used to cover the free surfaces of the samples to prevent formation of any twin bands within the bulk part. Figure 5.9 shows the optical micrographs of the front side of the micropillar in polarised light taken during the representative pair of elongation-contraction measurements for slow-moving TBs. Two twin variants with different orientations of the easy c-axis are distinguishable due to the contrast provided by the polarised light. The initial portion of the second twin variant (see Figure 5.9) was introduced by the manual application of a mechanical force ***F*** to the top part of the micropillar in a shear direction. Then magnetic field ***H*** was applied perpendicularly to the micropillar. This resulted in full elongation of the active part of the micropillar. The

active part had a length of about 100 µm (see Figure 5.9b), which corresponds to the maximum displacement of the micropillar's top of ~ 6 µm. The contracted state shown in Figure 5.9c was achieved by application of the same magnetic field pulse along the micropillar. Introduction of the initial "triangle" of the second twin variant was possible only with the slow-moving TBs. It was not possible to control the position of the fast-moving TBs with the manual application of mechanical force as they were too mobile; thus, we manipulated these TBs using a magnetic field. The application of a magnetic field along the micropillar allowed us to move the TB towards the top side and perpendicularly – towards the micropillar's bottom.

5.3.2 Displacement data analysis

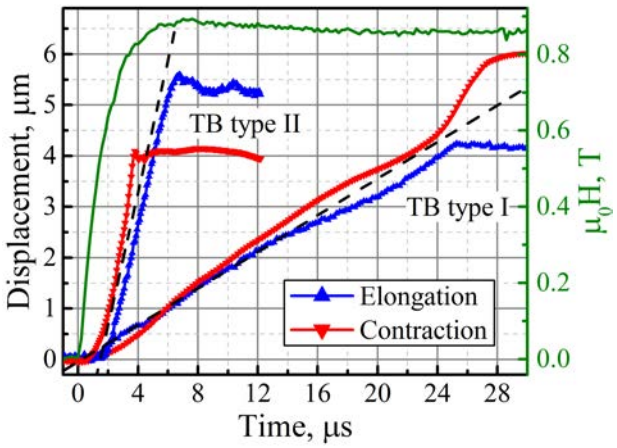

Figure 5.10: Two pairs of elongation-contraction measurements showing different actuation velocities, attributed to type I and type II TB motion. The absolute value of the displacement of the top side of the micropillar (left ordinate) and calculated magnetic field (right ordinate) are plotted versus time. The dashed lines represent the linear fits for displacements, the slopes of which provide actuation velocity values of 0.18 m/s for type I TB and of 1.3 m/s for type II.

Two well-defined actuation velocity patterns were recognised in the samples studied. Figure 5.10 shows two representative pairs of elongation-contraction measurements. The absolute value of the displacement of the top side of the micropillar (left ordinate) and the calculated magnetic field values (right ordinate) are plotted as functions of time. The speed difference of about an order allowed us to presume the type of TBs that were propagated during the experiment. Reflecting the similarities in actuation velocity values found earlier for bulk, mm-sized samples Saren et al. (2016a); Saren and Ullakko (2017), it was considered that slow-moving TBs were type I TBs and fast-moving TBs were type II. Average actuation velocities were found to be 0.18 m/s for type I TBs and 1.3 m/s for type II TBs, and corresponding TB motion speeds were 2.6 m/s and 20 m/s, respectively. In Figure 5.10, it can be seen that the absolute elongation of the micropillar for type I TBs is shorter than its absolute contraction because part of the second variant had already been introduced into the pillar. The difference in absolute displacements for type II TBs was possibly caused by the higher surface stress in the bottom part of the pillar, which pushed back the highly mobile twinning interface.

High-speed camera footage did not show any significant motion of the sample during TB propagation. This confirms that the recorded LDV signals are related to TB motion within the micropillar's active part only. We observed uniform shape change of the micropillar under exposure to a magnetic field pulse, which strongly suggests the possibility of a single TB motion. Observed shape change times correspond with the measured displacement data for the top side of the micropillar.

5.3.3 Twinning stress in Ni-Mn-Ga micropillars

Observed TB velocities are approximately 40% lower than in the bulk, mm-sized samples (4.2 m/s for type I TBs and 33 m/s for type II Saren et al. (2016a)). To determine the reason for such behaviour, we employed the flat punch indenter to measure the twinning stress (TS) required to move TBs of different types. We used a custom-made boron-doped diamond punch, with a diameter of 20 µm at its flat end, to push the micropillar from the top side. Prior to each measurement, the micropillar was fully elongated in a magnetic field (as shown in Figure 5.9b). The process was monitored by scanning electron microscope (SEM) to ensure that only a single TB was being moved. Compression of the micropillar was performed using a Hysitron PI 85 SEM PicoIndenter inside a FEI Quanta 3D FEG Dual Beam SEM. An Everhart Thornley detector was used to capture electron micrographs of the micropillar during the compression process. Errors in force and displacement measurement were 400 nN and 1 nm, respectively. We succeeded in recording multiple TS measurements for TBs of different types (see Figure 5.11).

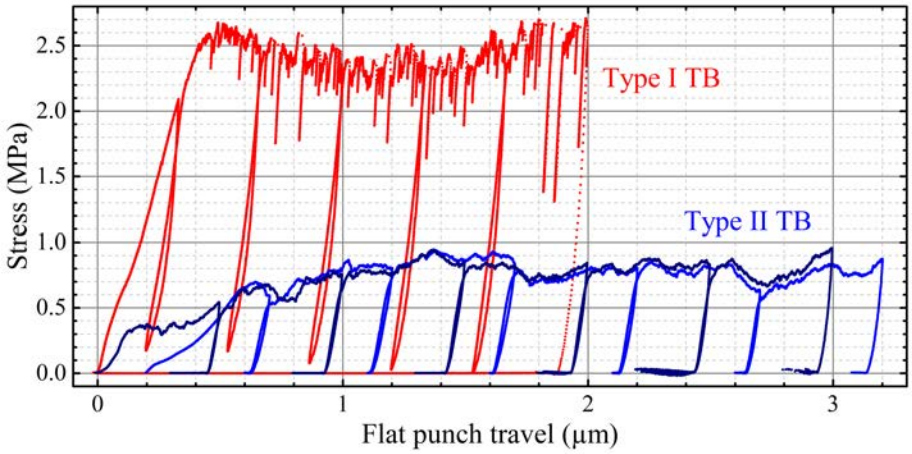

Figure 5.11: Twinning stress scatters plotted as functions of flat punch travel. Red scatter is considered to belong to slow-moving type I TB, blue and navy scatters – to fast-moving type II TB.

Highly mobile twinning interface (assumed to be TB type II), that remained in the micropillar after Laser Doppler Vibrometer (LDV) measurements, was studied first. We programmed the indentation machine to move the flat punch in consequent positive and shorter negative ramps, in order to diminish the influence of elastic bending stress on the TS measurement. Short negative ramps are visible in Figure 5.11 as stress decrease-increase loops. We recorded two force-displacement curves for that TB, the initial state was achieved by applying magnetic field

($\mu_0 H$ = 1.5 T) perpendicular to the micropillar. Then it was fully compressed mechanically and we introduced another TB by manual mechanical force application with KIMTECH Science Delicate Task Wiper. The created twinning interface was presumed to be TB type I due to a higher compressive force response with characteristic step-like behaviour.

For type I TBs, we recorded an average value of 2.3 ± 0.3 MPa and an average value of 0.8 ± 0.15 MPa for type II. Measurement error was defined as maximum deviation of TS curve from the average TS value in the "plateau" region. These TS values are less than the magnetic stress developed by the material in the saturating magnetic field (a typical σ_{mag} is about 3 MPa for the used composition Aaltio et al. (2016)), which ensures the feasibility of the MSM effect in Ni-Mn-Ga micropillars. According to the literature, five-layered Ni-Mn-Ga single crystals demonstrate TS values of ~ 1 MPa for type I TBs and ~ 0.05 − 0.3 MPa for type II TBs Straka et al. (2011); Sozinov et al. (2011). One of the reasons for the increased TS in the micropillars could be that the surface stresses inflicted by FIB milling were not fully removed by the electro-chemical etching. At the same time, we might be approaching the size limitation for the MIR Dunand and Müllner (2011). However, this issue requires further investigation, including fabrication of MSM microstructures of different sizes, and refinement of the surface removal technique.

5.3.4 Modelling single twin boundary motion in micropillars

In order to further understand the kinetics of type I and type TBs on the microscopic level, we employed the macroscopic variable-mass model describing single TB motion and developed in Saren and Ullakko (2017). We modelled the micropillar's elongation behaviour for a single TB motion, for both TB types, by numerical integration of Eq. 4.1, using standard numerical solving algorithms for ordinary differential equations found in MATLAB® R2017a software. The initial twin variants configuration was chosen according to Figure 5.9a, with $L_0 = 0$ and correspondent estimated initial mass of the moving variant, m_0 = 0.259 µg. The time-dependent magnetic field-induced stress, σ_{mag}, was modelled from the magnetic field pulse (calculated based on the measured current), with the maximum value of 3.05 MPa in saturation field. The dynamic twinning stress, σ_{res}, was modelled by a linear dependence for type I TB as $\sigma_1 = 2.0 + 0.4 \times V_{TB}$ (MPa), and by a power law for type II TB as $\sigma_2 = 0.9 + 0.026 \times V_{TB}^{1.4}$ (MPa), similarly to (Saren and Ullakko, 2017). Here we used quasi-static twinning stress values obtained from the twinning stress measurements conducted for one of the studied micropillars. The coefficients in the velocity-dependent terms were adjusted according to the average saturation TB velocity values using Eq. 4.2. The TB travel distance was limited to 64 µm, which corresponds to the active length of the micropillar of ~ 100 µm (starting from the initial "triangular"-like shape of the moving variant).

Figure 5.12 shows the measured and modelled micropillar elongation velocity and corresponding single TB motion speed for type I (a) and type II TBs (b). The delay of about 1µs for type II TB was most probably caused by extra surface stresses in the top corner of the micropillar from which the twinning interface starts its motion. Additionally, it includes the time it takes the TB to cross the laser beam in order to be detected. It should be noted that, in accordance with the model, the acceleration times required to reach saturation velocity were significantly lower for both types of TBs in the case of micropillars as compared with the mm-sized samples due to

the decrease of moving mass. This is seen most clearly in type II TB, for which the acceleration time is about 2 µs for micropillars, whereas for mm-sized samples it is ~ 20 µs Saren and Ullakko (2017). The model suggests a pronounced scaling effect. This effect occurs because the driving force scales proportionally to the dimension in squared units, whereas the mass scales proportionally to the dimension in cubed units. From the model, it follows that the initial acceleration for a smaller sample will increase nearly proportionally to the sample's dimension, which leads to a proportionally shorter acceleration time before the velocity saturates. Thus, the observed fast 5 µs-scale actuation of the micropillars is a result of both the high mobility of type II TBs and the scaling effect.

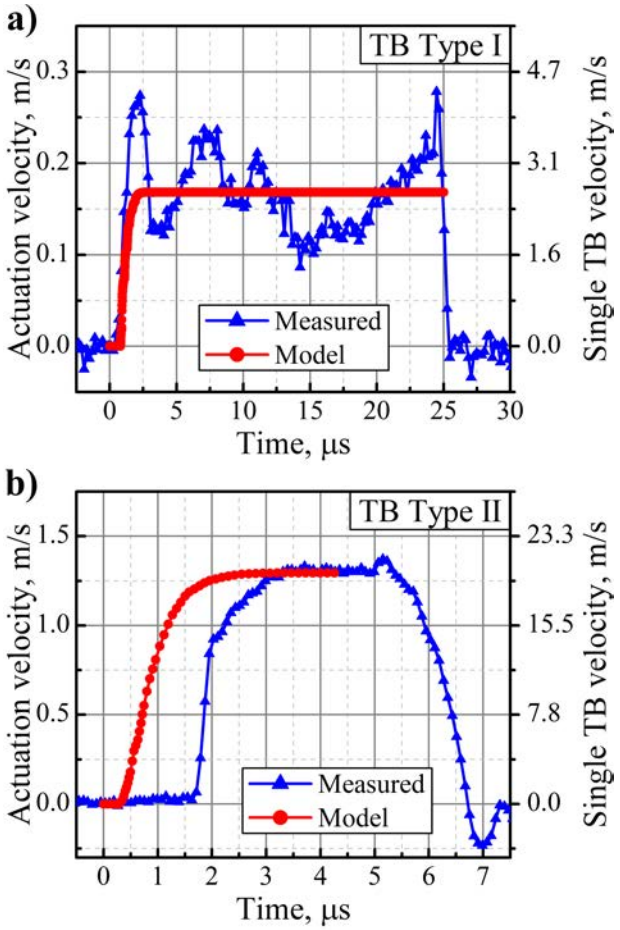

Figure 5.12: Measured and modelled micropillar elongation velocity (left ordinate) versus time for pulsed magnetic field actuation of type I (a) and type II (b) TBs. The right ordinates show corresponding TB velocity scales. Please note the difference in time and velocity scales between (a) and (b).

6 Conclusions and future research

The main scientific contributions of the Thesis are summarized as follows:

- The possibility of MIR in Ni-Mn-Ga foils thinned down to 1 μm was revealed. The absence thickness-related effects inhibiting magnetic-field-induced twin boundary motion was proven.
- Prototyping technology (based on FIB milling) for MSM microdevices was developed and proven in fabrication.
- Custom electropolishing technique was developed and tested. It allows for controlled stress-less electrochemical surface removal in complex metallic structures.
- Suitable parameters for aforementioned methods were found, which resulted in a magnetically active micropillar with low external switching field $\mu_0 H = 0.12$ T.
- Difference in dynamics of type I and type II twin boundaries at the microscale was found. The measured actuation velocities of 0.18 and 1.3 (m/s) for type I and type II TBs correspond strongly with the previously reported values for bulk, mm-sized samples.
- The actuation acceleration of micropillars was found to be approximately an order of magnitude larger than in bulk samples, demonstrating a well-pronounced scaling effect connected to the decrease of cross-section in actuated MSM crystals and therefore the reduction of moving mass.
- It was demonstrated that in micropillars giant MFIS of more than 6 % can be obtained in about 5 μs. This suggests the possibility of fabricating MSM-based microdevices with working frequencies of 100 kHz. We overcame previously reported bandwidth for MSM alloys by an order.
- Twinning stresses for single twin boundaries motion in micropillars were revealed to be $\sim$ 2.3 MPa for type I twins and $\sim$ 0.8 MPa for type II. It is suggested that increased twinning stress values (in comparison to the values for bulk material) are related to the incomplete removal of surface defects, but this issue requires further investigation.

The Author's future research will be focused on revealing the reasons for high twinning stress in micropillars and on developing suitable applications for MSM microdevices. The future research plan includes fabrication of micropillars and more complex structures of different sizes, studying the surface layer damaged by FIB milling and applying industrial manufacturing methods for MSM microdevices production, e.g. photo-resistive lithography and laser-based cutting.

References

Aaltio, I., Sozinov, A., Ge, Y., Ullakko, K., Lindroos, V.K., and Hannula, S.P. (2016). Giant Magnetostrictive Materials. *Reference Module in Materials Science and Materials Engineering*, p. 14.

Arzt, E. (1998). Size effects in materials due to microstructural and dimensional constraints: a comparative review. *Acta Materialia*, 46(16), pp. 5611–5626.

Bhattacharya, K., Li, B., and Luskin, M. (1999). The Simply Laminated Microstructure in Martensitic Crystals that Undergo a Cubic-to-Orthorhombic Phase Transformation. *Archive for Rational Mechanics and Analysis*, 149(2), pp. 123–154.

Burnett, T., Kelley, R., Winiarski, B., Contreras, L., Daly, M., Gholinia, A., Burke, M., and Withers, P. (2016). Large volume serial section tomography by Xe Plasma FIB dual beam microscopy. *Ultramicroscopy*, 161, pp. 119–129.

Chmielus, M., Witherspoon, C., Ullakko, K., Müllner, P., and Schneider, R. (2011). Effects of surface damage on twinning stress and the stability of twin microstructures of magnetic shape memory alloys. *Acta Materialia*, 59(8), pp. 2948–2956.

Dunand, D.C. and Müllner, P. (2011). Size Effects on Magnetic Actuation in Ni-Mn-Ga Shape-Memory Alloys. *Advanced Materials*, 23(2), pp. 216–232. ISSN 1521-4095.

Faran, E. and Shilo, D. (2016). Ferromagnetic Shape Memory Alloys – Challenges, Applications, and Experimental Characterization. *Experimental Techniques*, 40, pp. 1005–1031.

Giannuzzi, L. and Smith, N. (2011). TEM specimen preparation with plasma FIB Xe+ Ions. *Microscopy and Microanalysis*, 17(S2), p. 646.

Heczko, O., Scheerbaum, N., and Gutfleisch, O. (2009). Magnetic Shape Memory Phenomena. In: *Nanoscale Magnetic Materials and Applications*, pp. 399–439. Springer, Boston, MA. ISBN 9780387855981 9780387856001.

Heczko, O., Soroka, A., and Hannula, S.P. (2008). Magnetic shape memory effect in thin foils. *Applied Physics Letters*, 93(2), p. 022503.

Heczko, O., Vokoun, D., Kopeckỳ, V., and Beleggia, M. (2015a). Effect of magnetostatic interactions on twin boundary motion in NiMnGa Magnetic Shape Memory Alloy. *IEEE Magnetics Letters*, 6, pp. 1–4.

Heczko, O., Kopeckỳ, V., Fekete, L., Jurek, K., Kopeček, J., Straka, L., and Seiner, H. (2015b). Magnetic Domains and Twin Microstructure of Single Crystal Ni–Mn–Ga Exhibiting Magnetic Shape Memory Effect. *IEEE Transactions on Magnetics*, 51(11), pp. 1–4.

Hrnčíř, T., Lopour, F., Zadražil, M., Delobbe, A., Salord, O., and Sudraud, P. (2012). Novel plasma FIB/SEM for high speed failure analysis and real time imaging of large volume removal. In: *ISTFA: Conf. Proc. from the 38th Int. Symp. for Test. and Fail. Anal.*, p. 26.

Hubert, A. and Schäfer, R. (2008). *Magnetic domains: the analysis of magnetic microstructures*. Springer Science & Business Media.

Hubert, A., Calchand, N., Le Gorrec, Y., and Gauthier, J.Y. (2012). Magnetic shape memory alloys as smart materials for micro-positioning devices. *Advanced electromagnetics*, 1(2), pp. 75–84.

Ingram, D. and Armour, D. (1982). High dose implantation of xenon into nickel. *Nuclear Instruments and Methods in Physics Research*, 194(1-3), pp. 117–119.

Jaswon, M. and Dove, D. (1960). The crystallography of deformation twinning. *Acta Crystallographica*, 13(3), pp. 232–240.

Jenkins, C., Ramesh, R., Huth, M., Eichhorn, T., Pörsch, P., Elmers, H., and Jakob, G. (2008). Growth and magnetic control of twinning structure in thin films of Heusler shape memory compound Ni 2 MnGa. *Applied Physics Letters*, 93(23), p. 234101.

Kalimullina, E., Kamantsev, A., Koledov, V., Shavrov, V., Nizhankovskii, V., Irzhak, A., Albertini, F., Fabbrici, S., Ranzieri, P., and Ari-Gur, P. (2014). Magnetic shape memory microactuator. *Phys. status solidi (c)*, 11(5-6), pp. 1023–1025.

Kelley, R., Song, K., Van Leer, B., Wall, D., and Kwakman, L. (2013). Xe+ FIB milling and measurement of amorphous silicon damage. *Microscopy and Microanalysis*, 19(2), pp. 862–863.

Kohl, M., Schmitt, M., Backen, A., Schultz, L., Krevet, B., and Fähler, S. (2014a). Ni-Mn-Ga shape memory nanoactuation. *Applied Physics Letters*, 104(4), p. 043111.

Kohl, M., Gueltig, M., Pinneker, V., Yin, R., Wendler, F., and Krevet, B. (2014b). Magnetic shape memory microactuators. *Micromachines*, 5(4), pp. 1135–1160.

Lai, Y.W., Schäfer, R., Schultz, L., and McCord, J. (2010). Volume magnetic domain mirroring in magnetic shape memory crystals. *Applied Physics Letters*, 96(2), p. 022507.

Lanska, N., Söderberg, O., Sozinov, A., Ge, Y., Ullakko, K., and Lindroos, V. (2004). Composition and temperature dependence of the crystal structure of Ni–Mn–Ga alloys. *Journal of Applied Physics*, 95(12), pp. 8074–8078.

Likhachev, A.A. and Ullakko, K. (2000). Quantitative model of large magnetostrain effect in ferromagnetic shape memory alloys. *Eur. Phys. J. direct*, 1(1), pp. 1–9.

Ma, Y., Awaji, S., Watanabe, K., Matsumoto, M., and Kobayashi, N. (2000). X-ray diffraction study of the structural phase transition of Ni2MnGa alloys in high magnetic fields. *Solid State Communications*, 113(12), pp. 671–676.

Mayergoyz, I.D. (1999). *Handbook of giant magnetostrictive materials*. Elsevier.

Meeker, D.C. (2016). Finite Element Method Magnetics. *FEMM Ver. 4.2 x64*. url: `http://www.femm.info`.

Murakami, S., Wang, D., Mostaed, A., Khesro, A., Feteira, A., Sinclair, D.C., Fan, Z., Tan, X., and Reaney, I.M. (2018). High strain (0.4%) Bi (Mg2/3Nb1/3) O3-BaTiO3-BiFeO3 lead-free piezoelectric ceramics and multilayers. *Journal of the American Ceramic Society*.

Murray, S.J., Marioni, M., Allen, S.M., O'handley, R.C., and Lograsso, T.A. (2000). 6 % magnetic-field-induced strain by twin-boundary motion in ferromagnetic Ni–Mn–Ga. *Applied Physics Letters*, 77(6), pp. 886–888.

Musiienko, D., Saren, A., and Ullakko, K. (2017). Magnetic shape memory effect in single crystalline Ni-Mn-Ga foil thinned down to 1 μm. *Scripta Materialia*, 139, pp. 152–154.

Nespoli, A., Besseghini, S., Pittaccio, S., Villa, E., and Viscuso, S. (2010). The high potential of shape memory alloys in developing miniature mechanical devices: A review on shape memory alloy mini-actuators. *Sensors and Actuators A: Physical*, 158(1), pp. 149–160.

Nilsén, F., Aaltio, I., and Hannula, S.P. (2018). Comparison of magnetic field controlled damping properties of single crystal Ni-Mn-Ga and Ni-Mn-Ga polymer hybrid composite structures. *Composites Science and Technology*, 160, pp. 138–144.

Overholser, R.W., Wuttig, M., and Neumann, D.A. (1999). Chemical ordering in Ni-Mn-Ga Heusler alloys. *Scripta Materialia*, 40(10), pp. 1095–1102. ISSN 1359-6462.

Pérez-Checa, A., Feuchtwanger, J., Musiienko, D., Sozinov, A., Barandiaran, J., Ullakko, K., and Chernenko, V. (2017). High temperature Ni45Co5Mn25- xFexGa20Cu5 ferromagnetic shape memory alloys. *Scripta Materialia*, 134, pp. 119–122.

Pérez-Checa, A., Musiienko, D., Saren, A., Soroka, A., Feuchtwanger, J., Sozinov, A., Barandiaran, J., Ullakko, K., and Chernenko, V. (2019). Study of the critical parameters for magnetic field-induced strain in high temperature Ni-Mn-Ga-Co-Cu-Fe single crystals. *Scripta Materialia*, 158, pp. 16–19.

Reinhold, M., Kiener, D., Knowlton, W.B., Dehm, G., and Müllner, P. (2009). Deformation twinning in Ni–Mn–Ga micropillars with 10M martensite. *Journal of Applied Physics*, 106(5), p. 053906.

Saren, A., Musiienko, D., Smith, A., and Ullakko, K. (2016a). Pulsed magnetic field-induced single twin boundary motion in Ni–Mn–Ga 5M martensite: a laser vibrometry characterization. *Scripta Materialia*, 113, pp. 154–157.

Saren, A., Nicholls, T., Tellinen, J., and Ullakko, K. (2016b). Direct observation of fast-moving twin boundaries in magnetic shape memory alloy Ni–Mn–Ga 5 M martensite. *Scripta Materialia*, 123, pp. 9–12.

Saren, A. and Ullakko, K. (2017). Dynamic twinning stress and viscous-like damping of twin boundary motion in magnetic shape memory alloy Ni-Mn-Ga. *Scripta Materialia*, 139, pp. 126–129.

Saren, A., Musiienko, D., Smith, A., Tellinen, J., and Ullakko, K. (2015). Modeling and design of a vibration energy harvester using the magnetic shape memory effect. *Smart Materials and Structures*, 24(9), p. 095002.

Seiner, H., Straka, L., and Heczko, O. (2014). A microstructural model of motion of macro-twin interfaces in Ni–Mn–Ga 10 M martensite. *Journal of the Mechanics and Physics of Solids*, 64, pp. 198–211.

Smith, A.R., Tellinen, J., and Ullakko, K. (2014). Rapid actuation and response of Ni–Mn–Ga to magnetic-field-induced stress. *Acta Materialia*, 80, pp. 373–379.

Söderberg, O., Ge, Y., Sozinov, A., Hannula, S., and Lindroos, V. (2005). Recent breakthrough development of the magnetic shape memory effect in Ni–Mn–Ga alloys. *Smart Materials and Structures*, 14(5), p. S223.

Sozinov, A., Lanska, N., Soroka, A., and Straka, L. (2011). Highly mobile type II twin boundary in Ni-Mn-Ga five-layered martensite. *Applied Physics Letters*, 99(12), p. 124103.

Sozinov, A., Soroka, A., Lanska, N., Rameš, M., Straka, L., and Ullakko, K. (2017). Temperature dependence of twinning and magnetic stresses in Ni46Mn24Ga22Co4Cu4 alloy with giant 12% magnetic field-induced strain. *Scripta Materialia*, 131, pp. 33–36.

Straka, L., Heczko, O., Seiner, H., Lanska, N., Drahokoupil, J., Soroka, A., Fähler, S., Hänninen, H., and Sozinov, A. (2011). Highly mobile twinned interface in 10 M modulated Ni–Mn–Ga martensite: Analysis beyond the tetragonal approximation of lattice. *Acta Materialia*, 59(20), pp. 7450–7463.

Ullakko, K., Chmielus, M., and Müllner, P. (2015). Stabilizing a fine twin structure in Ni–Mn–Ga samples by coatings and ion implantation. *Scripta Materialia*, 94, pp. 40–43.

Ullakko, K., Wendell, L., Smith, A., Müllner, P., and Hampikian, G. (2012). A magnetic shape memory micropump: contact-free, and compatible with PCR and human DNA profiling. *Smart Materials and Structures*, 21(11), p. 115020.

Ullakko, K. (1996). Magnetically controlled shape memory alloys: a new class of actuator materials. *Journal of Materials Engineering and Performance*, 5(3), p. 405.

Ullakko, K., Huang, J.K., Kantner, C., O'handley, R.C., and Kokorin, V.V. (1996). Large magnetic-field-induced strains in Ni2MnGa single crystals. *Applied Physics Letters*, 69(13), pp. 1966–1968.

Vasil′ev, A.N., Bozhko, A.D., Khovailo, V.V., Dikshtein, I.E., Shavrov, V.G., Buchelnikov, V.D., Matsumoto, M., Suzuki, S., Takagi, T., and Tani, J. (1999). Structural and magnetic phase transitions in shape-memory alloys $Ni_{2+x}Mn_{1-x}Ga$. *Physical Review B*, 59(2), pp. 1113–1120.

Webster, P.J., Ziebeck, K.R.A., Town, S.L., and Peak, M.S. (1984). Magnetic order and phase transformation in Ni2MnGa. *Philosophical Magazine B*, 49(3), pp. 295–310. ISSN 1364-2812.

Wilson, S.A., Jourdain, R.P., Zhang, Q., Dorey, R.A., Bowen, C.R., Willander, M., Wahab, Q.U., Al-hilli, S.M., Nur, O., Quandt, E., et al. (2007). New materials for micro-scale sensors and actuators: An engineering review. *Materials Science and Engineering: R: Reports*, 56(1-6), pp. 1–129.

Publication I

Musiienko, D., Saren, A., and Ullakko, K.
Magnetic shape memory effect in single crystalline Ni-Mn-Ga foil thinned down to 1 μm

Reprinted with permission from
Scripta Materialia,
Vol. 139, pp. 152–154, 2017

Scripta Materialia 139 (2017) 152–154

Contents lists available at ScienceDirect

Scripta Materialia

journal homepage: www.elsevier.com/locate/scriptamat

Regular Article

Magnetic shape memory effect in single crystalline Ni-Mn-Ga foil thinned down to 1μm

Denys Musiienko, Andrey Saren, Kari Ullakko*

Material Physics Laboratory, Lappeenranta University of Technology, Laitaatsillantie 3, Savonlinna 57170, Finland

ARTICLE INFO

Article history:
Received 19 May 2017
Received in revised form 8 June 2017
Accepted 15 June 2017
Available online xxxx

Keywords:
Ferromagnetic shape memory
Twinning
Magnetic domains
Thin films
Ni-Mn-Ga

ABSTRACT

We report on observation of magnetic-field-induced twin variant reorientation in a thin foil with variable thickness, fabricated from a bulk five-layered $Ni_{49.5}Mn_{28}Ga_{22.5}$ single crystal. Formation and motion of twinning interfaces in the foil were induced by magnetic fields of 0.6 T. The characteristic "labyrinth" magnetic domain structure was fully retained down to 1 μm thickness. Dependence of the characteristic width of magnetic domains on the sample thickness followed a power law with the exponent of 2/3. The reported results indicate that micrometer-scale sized Ni-Mn-Ga devices, fabricated from a bulk, can be actuated by magnetic field.

Ni-Mn-Ga is known for its large reversible magnetic-field-induced strain (MFIS) of several percent, which is called magnetic shape memory (MSM) effect [1–3]. The mechanism behind the MSM effect is the magnetically induced reorientation (MIR) of the crystal lattice. Martensitic twin variants with the short crystallographic c-axis (axis of easy magnetization), oriented along the applied magnetic field, grow at the expense of other variants with different orientation. After the magnetic field is removed, the specimen retains its shape [4]. One of the most advantageous directions of the MSM-based applications development is the actuation at micro-scale [5]. In [6], large change of mechanical properties was predicted when the smallest dimension of a sample becomes comparable to the characteristic length relevant for the dislocation-mediation mechanism, which has an order of a micrometer. According to Dunand and Müllner, twinning is a disconnection-mediated process, which resembles in many ways dislocation-mediated processes, and its characteristic length is assumed to be of a similar order [7]. They expect an increase of the twinning stress with decreasing size (i.e. with decreasing film thickness), which would hinder MFIS.

Two methods for fabrication of micrometer-sized Ni-Mn-Ga specimens were developed and studied: (1) epitaxial film growth on a substrate [8–10] and (2) machining from a bulk [11–13]. The first method allows to create nanometer-sized thin films with the crystal structure inherited from the substrate. Foils fabricated by the first method exhibited only multi-variant twinning structures [9,10]. Another drawback of the first method is the difficulty of the chemical composition control, whereas the second method allows to maintain the composition of the bulk in smaller size samples. So far, the thinnest foil produced by the second method, which was studied in a single variant twinning state, was 80 μm thick [11].

The goal of the present study is to investigate MIR of the crystal lattice in Ni-Mn-Ga samples with the thickness down to 1μm, prepared using the second method.

A high precision wire saw (Princeton Scientific Corp., WS-22) was used to cut specimens with a shape of 90° disk sector with thickness of 150 ± 20 μm, from a $Ni_{49.5}Mn_{28}Ga_{22.5}$ oriented single crystalline bar of 20 mm in diameter. Austenite transformation of that alloy occurs at 303 K, and the MFIS in the 5M martensite phase is approximately 6% at RT. First, the specimens where electropolished at 273 K in an electrolyte solution of 3 parts of 60% HNO_3 mixed with 1 part of ethanol at a constant voltage of 20 V during 20 s. Then, a custom electropolishing technique was used to make a thinned edge. The specimen was glued with a conductive glue onto an anode, and a cathode (with the shape of a rod of 1.6 mm in diameter) was placed ~1 mm above the sample surface near the edge. The electrolyte flux created by a magnetic stirrer was washing the open surface of the specimen, while an adjustable pulsed voltage was applied between the anode and the cathode. The voltage function had a shape of square pulses of 12 V amplitude and 50% duty cycle at 60 Hz. As a

* Corresponding author.
E-mail address: kari.ullakko@lut.fi (K. Ullakko).

http://dx.doi.org/10.1016/j.scriptamat.2017.06.027
1359-6462/

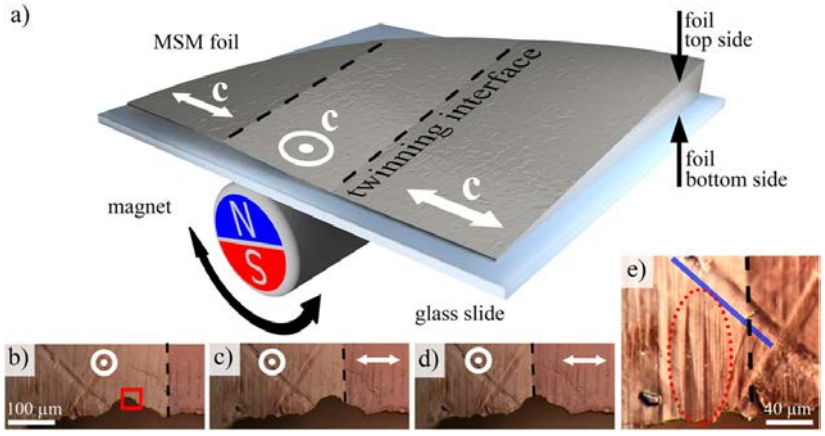

Fig. 1. (a) Schematic view of the experimental setup used to induce the magnetically induced reorientation of twin variants in the samples. (b–e) Optical micrographs of the bottom side of the specimen in polarized light showing few subsequent steps of the twinning interface motion through the thinnest edge of the sample, initiated by rotation of the magnet. The twinning interface is denoted by the dashed line. White arrows indicate the direction of the easy c-axis in the twin variants. Red square highlights the chosen region studied by AFM/MFM. (e) Optical micrograph representing the appearance of multiple variants (see the area highlighted by the red dots) constrained by a surface defect (denoted by the blue line). (For interpretation of the references to colour in this figure legend, the reader is referred to the web version of this article.)

result, the foil remained its initial dimensions, and a part of it, located under the cathode, was thinned from the top side, while the bottom side remained flat.

A diametrically magnetized cylindrical magnet (ø6.35 × 25.4 (mm), NdFeB, Grade N42) with a maximal surface field of ~0.6 T was used to produce MIR of twin variants in the studied sample, as shown in Fig. 1a. The optical images (see Fig. 1b–d) represent the motion of a twinning interface through the thinnest part of the sample, caused by a continuous rotation of the magnet. The observed MIR of twin variants is possible due to magnetic field distribution in the Ni-Mn-Ga foil created by the magnet, which is discussed in [14]. The transformation strain was measured to be 6 ± 1%. *A video demonstrating the MSM effect in the thin part of the studied foil is available online as supplementary material "Video 1".*

Fig. 1e shows multiple twin variants, which appeared and grew in a small region, separated from the thicker part of the foil by a surface defect. These twins were constrained by the aforementioned defect at the thicker part of the region with the thickness measured to be 12 ± 2 μm, while they were freely expanded at the ~ 1 μm edge of the foil by the applied magnetic field. The behavior of the crystal structure in this region indicates that there are no signs of inhibition of MIR of the crystal lattice, related to the small, ~ 1 μm, thickness

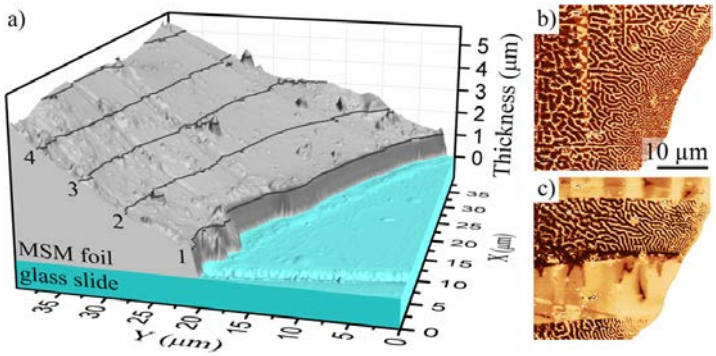

Fig. 2. (a) AFM topography map of the top side of the thinned edge of the foil (see the chosen region marked in Fig. 1b). Glass slide surface serves as zero-level of the thickness profile, isolines are shown for each 1μm of the thickness. Front face of the picture is artificially coloured for the ease of visual perception. (b,c) MFM scans of the same region: (b) single variant state with easy magnetization axis perpendicular to the plain of the scan; (c) multi-variant state. Magnetic domains are arranged in a characteristic "labyrinth" structure. Their characteristic width increases with the thickness of the foil from the right to the left. (For interpretation of the references to colour in this figure legend, the reader is referred to the web version of this article.)

of the foil. *A video, demonstrating the above observation, is available online as supplementary material "Video 2".*

To characterize the shape and magnetic domain (MD) structure of the specimen's thinnest edge, an atomic force microscope (AFM) with magnetic force microscopy (MFM) feature (ParkSystems, XE 7) was used. Initially, the sample was switched to the state with the c-axis perpendicular to the surface of the foil. Roughness of the bottom surface was evaluated by AFM to be in the range of 0.2 μm near the thinnest edge. After that, the bottom side of the sample was glued to the glass slide in saturating magnetic field. The purpose of the magnetic field was to keep the sample in a single-variant state and to press the sample against the glass surface. The 3D view of the AFM scan of the chosen area (see the red rectangle in Fig. 1b), taken from the top side of the foil, is shown in Fig. 2a. Thickness of the edge of the tapered sample was measured to be 1 μm including the glue layer. After that, the specimen was detached from the glass by dissolving the glue in acetone. As reported in [15], a bulk Ni-Mn-Ga exhibits a characteristic "labyrinth" MD structure. The MFM scans from the top side of the chosen region in a single- (Fig. 2b) and multi-variant state (Fig. 2c) show that the studied sample has the same MD structure. This observation proves that the magnetic structure of a bulk material is retained down to the micron scale in the studied Ni-Mn-Ga alloy.

In order to improve the quality of the magnetic structure image, we made MFM scan from the bottom side of the chosen area, shown in the inset of Fig. 3a. The thickness profile of the thinnest edge of the foil derived from the AFM scan (Fig. 2a) is presented in Fig. 3a. It was characterized to be linear with a slope of 0.12 ± 0.01 μm/μm. The characteristic width of MDs, δ, was calculated from the MFM image and is shown in Fig. 3b as a function of the foil thickness. Data

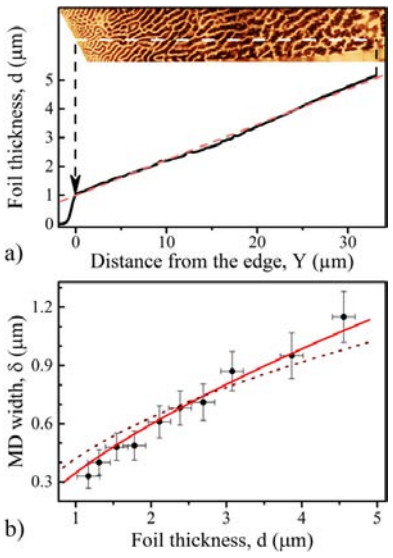

Fig. 3. (a) MFM image taken from the bottom side of the foil (inset) and corresponding foil thickness profile obtained from the AFM scan (Fig. 2a). Dashed red line is a linear fit with an intercept value of 1 μm and a slope of 0.12 μm/μm. (b) Magnetic domain characteristic width, δ, dependence on the thickness of the foil, d. Dashed and solid fitting curves are power functions with the exponents of 1/2 and 2/3, correspondingly (see Eq. (1)). (For interpretation of the references to colour in this figure legend, the reader is referred to the web version of this article.)

was fitted by the following power function used for magnetically anisotropic thin films [16]:

$$\delta = \xi_\alpha (d - d_0)^\alpha, \quad (1)$$

where d is the film thickness, d_0 - thickness error, and ξ_α - a coefficient related to the anisotropy and exchange energies of the material. Theoretical value of α equals to 1/2 for a thin film and 2/3 for a thick film in which domains branching occurs [16]. For the presented data, considering $d_0 \leqslant 0.2$ μm, it was found that the value of 2/3 for α provides better fit (see Fig. 3b). This indicates that MDs might have a branched micro-structure down to foil thickness of 1 μm. In the presented MFM images, the branching of the domains is clearly observable starting from the foil thickness of 2.5 μm. We suppose that for smaller thicknesses, branching is not visible due to the limitations of the MFM scan resolution.

In summary, magnetic shape memory foil tapered down to 1μm was fabricated from a bulk five-layered Ni-Mn-Ga single crystal. It was shown that twinning interfaces can be moved by a magnetic field of 0.6 T even in the thinnest region of the foil. The characteristic "labyrinth" magnetic domain structure was clearly observed down to 1 μm thickness. The characteristic width of magnetic domains was found to decrease with the thickness of the foil, following a power law with the exponent of 2/3. No thickness-related effects, inhibiting magnetic-field-induced twin boundary motion, were observed down to the micrometer-scale foil thicknesses. Our findings imply the possibility of manufacturing of MSM-effect-based devices, such as actuators and sensors, with micrometer-scale active parts made from Ni-Mn-Ga alloys.

The authors thank Oleksii Sozinov for fruitful discussions and Elmar Bernhardt for the design of the electropolishing controller. This work was supported by the Academy of Finland (grant numbers 277996 and 287016).

Supplementary data to this article can be found online at http://dx.doi.org/10.1016/j.scriptamat.2017.06.027.

References

[1] K. Ullakko, J. Mater. Eng. Perform. 5 (1996) 405.
[2] K. Ullakko, J.K. Huang, C. Kantner, R.C. Ohandley, V.V. Kokorin, Appl. Phys. Lett. 69 (1996) 1966–1968.
[3] S.J. Murray, M. Marioni, S.M. Allen, R.C. O'handley, T.A. Lograsso, Appl. Phys. Lett. 77 (2000) 886–888.
[4] I. Aaltio, A. Sozinov, Y. Ge, K. Ullakko, V.K. Lindroos, S.-P. Hannula, Reference Module in Materials Science and Materials Engineering (2016) 14.
[5] A. Nespoli, S. Besseghini, S. Pittaccio, E. Villa, S. Viscuso, Sensors Actuators A Phys. 158 (2010) 149–160.
[6] E. Arzt, Acta materialia 46 (1998) 5611–5626.
[7] D.C. Dunand, P. Müllner, Adv. Mater. 23 (2011) 216–232.
[8] V. Chernenko, R.L. Anton, M. Kohl, M. Ohtsuka, I. Orue, J. Barandiaran, J. Phys. Condens. Matter 17 (2005) 5215.
[9] M. Thomas, O. Heczko, J. Buschbeck, Y.W. Lai, J. McCord, S. Kaufmann, L. Schultz, S. Fähler, Adv. Mater. 21 (2009) 3708–3711.
[10] P. Ranzieri, M. Campanini, S. Fabbrici, L. Nasi, F. Casoli, R. Cabassi, E. Buffagni, V. Grillo, C. Magén, F. Celegato, et al. Adv. Mater. 27 (2015) 4760–4766.
[11] O. Heczko, A. Soroka, S.-P. Hannula, Appl. Phys. Lett. 93 (2008) 022503.
[12] V. Pinneker, R. Yin, C. Eberl, A. Sozinov, Y. Ezer, M. Kohl, J. Alloys Compd. 577 (2013) S358–S361.
[13] G. Murasawa, S.R. Yeduru, M. Kohl, Opt. Lasers Eng. 87 (2016) 139–145.
[14] K. Ullakko, L. Wendell, A. Smith, P. Müllner, G. Hampikian, Smart Mater. Struct. 21 (2012) 115020.
[15] O. Heczko, V. Kopecký, L. Fekete, K. Jurek, J. Kopeček, L. Straka, H. Seiner, IEEE Trans. Magn. 51 (2015) 1–4.
[16] A. Hubert, R. Schäfer, Magnetic Domains: The Analysis of Magnetic Microstructures, Springer Science & Business Media. 2008.

Publication II

Musiienko, D., Straka, L., Klimša, L., Saren, A., Sozinov, A., Heczko, O., Ullakko, K.
Giant magnetic-field-induced strain in Ni-Mn-Ga micropillars

Reprinted with permission from
Scripta Materialia
Vol. 150, pp. 173–176, 2018

Scripta Materialia 150 (2018) 173–176

Contents lists available at ScienceDirect

Scripta Materialia

journal homepage: www.elsevier.com/locate/scriptamat

Regular article

Giant magnetic-field-induced strain in Ni-Mn-Ga micropillars

Denys Musiienko[a], Ladislav Straka[b], Ladislav Klimša[b], Andrey Saren[a], Alexei Sozinov[a], Oleg Heczko[b], Kari Ullakko[a,*]

[a] Material Physics Laboratory, Lappeenranta University of Technology, Laitaatsillantie 3, 57170 Savonlinna, Finland
[b] Institute of Physics of the Czech Academy of Sciences, Na Slovance 2, 182 21 Prague 8, Czech Republic

ARTICLE INFO

Article history:
Received 16 February 2018
Received in revised form 13 March 2018
Accepted 13 March 2018
Available online xxxx

Keywords:
Ferromagnetic shape memory
Twinning
MEMS
Focused ion beam
Micro-magneto-mechanical systems

ABSTRACT

We report on the observation of fully reversible magnetic-field-induced strain of 6% in a single-crystalline micropillar fabricated from a bulk $Ni_{50}Mn_{28.5}Ga_{21.5}$ single crystal. Xe plasma source focused ion beam column milling technology was used to machine 50 × 50 × 100 μm^3 cuboid pillars. The removal of about 2 μm of ion-beam-damaged surface layer enabled magnetic field actuation in pillars. Our results demonstrate the feasibility of manufacturing of micrometre-sized magnetic shape memory actuators by focused ion beam technique.

Magnetic shape memory (MSM) alloys [1,2] exhibit large reversible magnetic-field-induced strain (MFIS) in the martensite phase at a high speed [3]. MSM alloys offer prospects for novel applications and embody a new mechanism for magnetic-to-mechanical energy conversion. Therefore, they have received considerable attention in scientific research during the past decades [4,5,6,7]. The mechanism behind the MSM effect is the magnetically induced reorientation (MIR) of the crystal lattice by twin boundary (TB) motion [2,8,9]. Scaling down to microscale became one of the most advantageous development directions in the field [7,10]. Similar to microelectromechanical systems (MEMS), here the key idea is to replace existing complex machinery by magneto-mechanically active materials.

The MSM alloys were previously successfully used in micro- and nanoactuators as shape memory material: Ni-Mn-Ga beams exhibited reversible thermal and thermomagnetic shape memory effect down to 100 nm [11,12,13]. The operating principle there is based on the austenite-martensite phase transformation induced by heating and/or by magnetic field application. However, to obtain the true advantage of the MSM effect, especially the fast and large actuation simultaneously, MIR must be employed. Thus, microactuators should be manufactured from the single-crystalline MSM material.

Recently, we have shown that if one dimension of the Ni-Mn-Ga single crystal is decreased to 1 μm, the MIR is not hindered [14]. In the present study, we make an important step in the research on the microstructural engineering of magneto-mechanically active materials. We report on the investigation of a micropillar, which was created by decreasing two dimensions of a bulk structure. Focused ion beam (FIB) milling has been used as one of the most advanced microstructure prototyping technologies.

Previous studies of MSM micropillars fabricated by FIB milling showed that the mechanical stress required for the twin variant reorientation (usually called the twinning stress) is significantly higher than the magnetic stress that could be produced by the material [6,9,15]. One exception is the work by Jenkins et al. [16], who reported the rearrangement of twin variants in a magnetic field, which was, however, irreversible. Two major reasons for high twinning stress were proposed: surface damage (by Ga^+ ion implantation) and size effect [6,15]. Because the latter was shown to be insignificant down to 1 μm [14], the surface damage stress induced by ion beam milling should mainly affect the MIR in micrometre-sized pillars, similarly to the bulk material with surface stresses introduced by various methods [17,18].

In the present study, electron-cyclotron-resonance-generated Xe plasma over Ga liquid metal ion source was chosen because of the significant reduction in the depth of ion implantation, thinner damaged layer and an order of magnitude higher milling speed [19,20,21,22,23]. To provide a controlled smooth removal of the surface deformation layer, the electropolishing technique described

* Corresponding author.
E-mail address: kari.ullakko@lut.fi (K. Ullakko).

https://doi.org/10.1016/j.scriptamat.2018.03.020
1359-6462/

in [14] was used. All the electrochemical etching procedures were made in an electrolyte mixture of 1 part of 60% HNO_3 and 3 parts of denatured ethanol kept at 253 K. Pulse width modulated voltage (at 50 Hz) was applied between the sample (anode) and acid-resistant stainless steel spiral (cathode) immersed into the electrolyte solution, which was constantly mixed using a magnetic chemical stirrer. All the electro-polishing procedures were controlled by voltage modulation.

Three cuboid samples (6.5 × 2.5 × 1 mm^3) were cut from an $Ni_{50}Mn_{28.5}Ga_{21.5}$ single crystal grown in Adaptamat Ltd. using a precision wire saw (Princeton Scientific Corp., WS-22) and then mechanically polished. The chosen single crystal exhibited five-layered modulated martensite structure at room temperature. Martensite transformation and Curie temperatures of the crystal were $T_M = 321$ K, $T_A = 327$ K and $T_C = 371$ K, and maximum possible compressive MFIS derived from the lattice parameters was $1 - c/a = 6.3\%$ [24]. Prior to machining, the specimens were electropolished and reoriented to the single-variant state by the application of a magnetic field of 1.4 T, which is higher than the saturation field [6]. The FIB milling was performed using fully integrated Xe plasma source FIB using scanning electron microscope (FIB-SEM) TESCAN FERA3 GM. The process was monitored by secondary electrons (SE) imaging (Everhart-Thornley SE detector) at 5 kV / 500 pA for SEM and 30 kV / 10 nA for FIB-generated SE. Rough 100 µm deep milling at 30 kV / 300 nA was followed by more precise pillar polishing at 30 kV / 100 nA, which gave a final shape to the pillar (see Fig. 1).

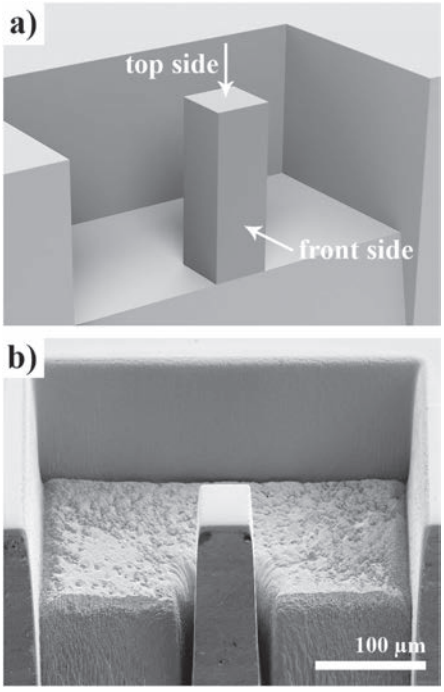

Fig. 1. (a) Schematic view of Ni-Mn-Ga single-crystalline micropillar and (b) top-front view captured by SE detector in SEM after FIB milling procedure. In (a), the top and front sides of the pillar are marked with arrows.

Front side of the pillar was not directly exposed to the plasma beam intentionally. The micropillar had the shape of a truncated pyramid, with a height of 108µm and rectangular parallel bases with sizes of approximately 50 × 50 µm (bottom) and 48 × 43 µm (top). The deviation in the size is due to the non-Gaussian shaped FIB with significant beam tails.

Optical micrographs of the pillar under polarised light after FIB machining are presented in Fig. 2a, b. A fine twin structure was observed on the top side (Fig. 2a) because of the surface stresses induced by ion beam milling to other faces of the pillar. According to [23], the thickness of a damaged layer should be approximately 100 nm. Therefore, the sample with the micropillar was electropolished gradually in steps of 10 s. After each procedure of the surface removal, the pillar was tested in the magnetic field of 1.1 T. It was found that after a total duration of 90 s, the pillar showed a fully reversible MIR of twin variants in the field. Optical views of the micropillar after electrochemical etching are shown in Fig. 2c, d. Comparison of the pictures of the pillar before and after electropolishing showed that the thickness of the removed surface layer was in the range of 0.5 to 4 µm, with an average of approximately 2 µm. Because of the specific electric field distribution caused by the complex structure of the sample, the surface layers removed from the edges and the top face of the pillar were thicker than the ones removed from the pillar bottom and bulk specimen.

Prior to MIR investigation in the micropillar, a magnetic field of 1.5 T was applied to the sample along longest dimension of the

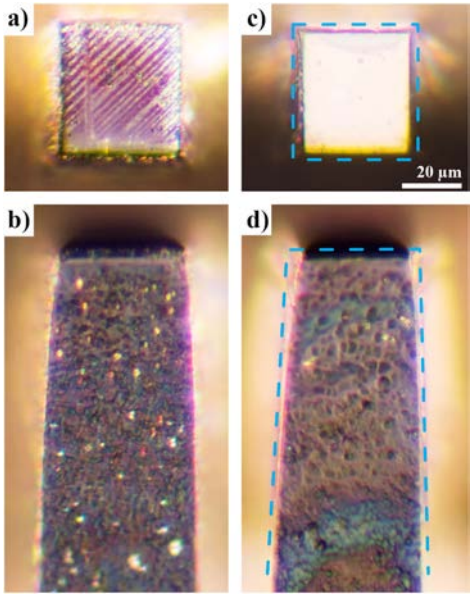

Fig. 2. (a, b) Ni-Mn-Ga micropillar top and front sides after fabrication and (c, d) after electropolishing captured by optical microscope under polarised light. Two-variant micro-structure visible in (a) is caused by surface stresses induced by the ion-beam milling. A single-variant state is observed in (c) and (d) after the damaged surface layer was removed by electro-chemical etching. The contour of the sample after fabrication from (a) and (b) is indicated by dashed line in (c) and (d) for comparison. All micrographs have the same scale.

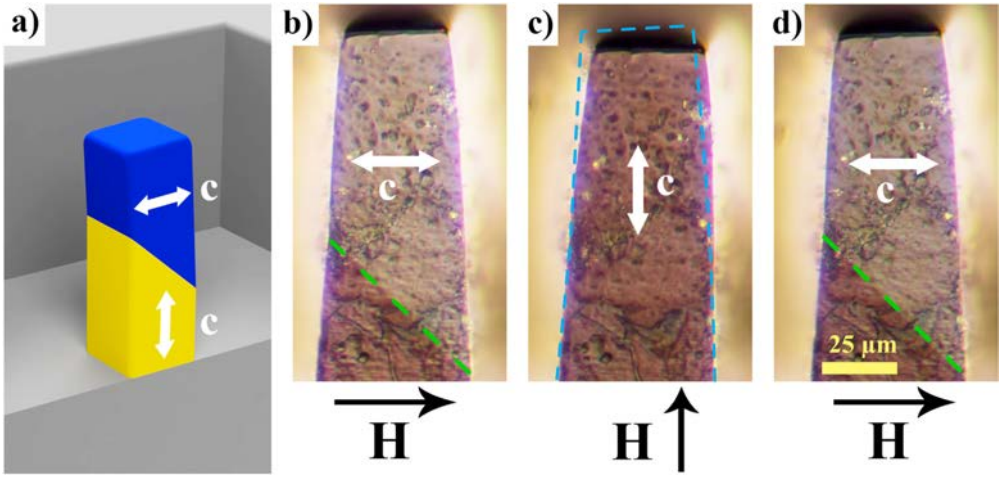

Fig. 3. (a) Schematic view and (b–d) front face optical images demonstrating magnetically induced reorientation of twin variants in Ni-Mn-Ga micropillar. Directions of magnetic field ($\mu_0 H = 0.5$ T) applied before taking each picture, are denoted by black arrows. Twin variants are distinguished by polarised light contrast. Twin boundaries in (b) and (d) are indicated by green dashed lines. White arrows show the direction of c-axis in the micropillar. Pillar contour from (b) is denoted by dashed cyan line in (c) for reference. All micrographs have the same scale. (For interpretation of the references to color in this figure legend, the reader is referred to the web version of this article.)

micropillar to reorient it to the single-variant state. The sample was glued with a super glue onto the sample holder to ensure that TBs will move only within the pillar and will not be driven by the MIR of twin variants in the bulk. The sample holder was mounted on a rotatable stage inside the electromagnet so that the front side of the pillar was observable by the microscope.

There are two possible TB orientations for the longitudinal micropillar actuation. Fig. 3a represents the schematic view of the first orientation. MIR of the micropillar was performed by the repeated application of the magnetic field ($\mu_0 H = 0.5$ T) in two perpendicular directions. Fig. 3b shows the optical micrograph of the micropillar after the magnetic field was applied perpendicularly to the longest dimension of the micropillar. Then, the field was applied along the micropillar, which resulted in a full MIR (Fig. 3c). The change in the length of the active part of the pillar was optically measured to be 6 ± 0.5%. Fig. 3d shows that the MIR is fully reversible and repeatable. The lowest external field that causes the TB motion in the pillar was measured to be 0.12 T.

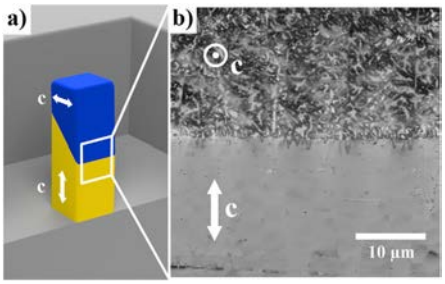

Fig. 4. (a) Schematic view of the Ni-Mn-Ga micropillar after changing its twinning structure and (b) magnetic force microscopy image of the highlighted region in (a). White arrows show the direction of the easy magnetisation c-axis.

The second TB orientation was induced by repeated magnetic field application in another pair of perpendicular directions (a normal to the front and a normal to the top sides of the pillar). Fig. 4a shows the schematic view of such TB orientation. Magnetic field microscopy image of the highlighted region of size $40 \times 40\,\mu m^2$ in Fig. 4a is presented in Fig. 4b. We observed a branched magnetic domain (MD) structure in the martensite variant with the easy magnetisation axis perpendicular to the surface and a 'needle-like' MD structure in the variant with the c-axis laying in the surface plane [25]. The observed MD structure is inherited from the bulk material [26]. This confirms that magnetic properties of the studied object are similar to those of the bulk.

In conclusion, we presented for the first time the way how magneto-mechanically active microdevices can be manufactured from the bulk Ni-Mn-Ga single crystal using standard techniques. We found suitable parameters for focused-ion-beam milling and electrochemical etching, which resulted in a magnetically active micropillar with low external switching field $\mu_0 H$ of 0.12 T. The thickness of ion-beam-damaged layer was found to be smaller than 2 µm. These important results indicate that magnetically active micro-structures based on the MSM alloys could be fabricated on the scale of several micrometres.

Acknowledgments

This work was supported by the Academy of Finland (grant number 287016). This project has received funding from the European Union's Horizon 2020 research and innovation programme under grant agreement No. 701867 – FUNMAH. The authors acknowledge the Czech Science Foundation (grant No. 16-00043S) and in part the MEYS CR FUNBIO CZ.2.16/3.1.00/21568 (SEM purchase), LO1409 and LM2015088 projects (SEM maintenance).

References

[1] K. Ullakko, J. Mater. Eng. Perform. 5 (1996) 405.
[2] K. Ullakko, J.K. Huang, C. Kantner, R.C. O'Handley, V.V. Kokorin, Appl. Phys. Lett. 69 (1996) 1966–1968.
[3] A. Saren, T. Nicholls, J. Tellinen, K. Ullakko, Scr. Mater. 123 (2016) 9–12.
[4] A. Sozinov, A. Likhachev, N. Lanska, K. Ullakko, Appl. Phys. Lett. 80 (2002) 1746–1748.
[5] S.J. Murray, M. Marioni, S.M. Allen, R.C. O'Handley, T.A. Lograsso, Appl. Phys. Lett. 77 (2000) 886–888.
[6] D.C. Dunand, P. Müllner, Adv. Mater. 23 (2011) 216–232.
[7] E. Faran, D. Shilo, Exp. Tech. 40 (2016) 1005–1031.
[8] A.A. Likhachev, K. Ullakko, Eur. Phys. J. direct 1 (2000) 1–9.
[9] I. Aaltio, A. Sozinov, Y. Ge, K. Ullakko, V.K. Lindroos, S.-P. Hannula, Ref. Module in Mater. Sci. Mater. Eng. (2016) 14.
[10] A. Nespoli, S. Besseghini, S. Pittaccio, E. Villa, S. Viscuso, Sens. Actuators, A 158 (2010) 149–160.
[11] M. Kohl, M. Schmitt, A. Backen, L. Schultz, B. Krevet, S. Fähler, Appl. Phys. Lett. 104 (2014) 043111.
[12] M. Kohl, M. Gueltig, V. Pinneker, R. Yin, F. Wendler, B. Krevet, Micromachines 5 (2014) 1135–1160.
[13] E. Kalimullina, A. Kamantsev, V. Koledov, V. Shavrov, V. Nizhankovskii, A. Irzhak, F. Albertini, S. Fabbrici, P. Ranzieri, P. Ari-Gur, Phys. Status Solidi C 11 (2014) 1023–1025.
[14] D. Musiienko, A. Saren, K. Ullakko, Scr. Mater. 139 (2017) 152–154.
[15] M. Reinhold, D. Kiener, W.B. Knowlton, G. Dehm, P. Müllner, J. Appl. Phys. 106 (2009) 053906.
[16] C. Jenkins, R. Ramesh, M. Huth, T. Eichhorn, P. Pörsch, H. Elmers, G. Jakob, Appl. Phys. Lett. 93 (2008) 234101.
[17] M. Chmielus, C. Witherspoon, K. Ullakko, P. Müllner, R. Schneider, Acta Mater. 59 (2011) 2948–2956.
[18] K. Ullakko, M. Chmielus, P. Müllner, Scr. Mater. 94 (2015) 40–43.
[19] D. Ingram, D. Armour, Nucl. Instrum. Methods Phys. Res. 194 (1982) 117–119.
[20] L. Giannuzzi, N. Smith, Microsc. Microanal. 17 (2011) 646.
[21] T. Hrnčíř, F. Lopour, M. Zadražil, A. Delobbe, O. Salord, P. Sudraud, Novel plasma FIB/SEM for high speed failure analysis and real time imaging of large volume removal, ISTFA: Conf. Proc. from the 38th Int. Symp. for Test. and Fail. Anal., 2012, pp. 26.
[22] R. Kelley, K. Song, B. Van Leer, D. Wall, L. Kwakman, Microsc. Microanal. 19 (2013) 862–863.
[23] T. Burnett, R. Kelley, B. Winiarski, L. Contreras, M. Daly, A. Gholinia, M. Burke, P. Withers, Ultramicroscopy 161 (2016) 119–129.
[24] A. Sozinov, N. Lanska, A. Soroka, L. Straka, Appl. Phys. Lett. 99 (2011) 124103.
[25] Y.-W. Lai, R. Schäfer, L. Schultz, J. McCord, Appl. Phys. Lett. 96 (2010) 022507.
[26] O. Heczko, V. Kopecký, L. Fekete, K. Jurek, J. Kopeček, L. Straka, H. Seiner, IEEE Trans. Magn. 51 (2015) 1–4.

Publication III

Musiienko, D., Straka, L., Klimša, L., Saren, A., Sozinov, A., Heczko, O., Ullakko, K.
Magnetic-field-induced actuation of Ni-Mn-Ga micro-pillars

Reprinted with permission from Dr. Hubert Borgmann
Proceedings of 16th International Conference on New Actuators (ed. H. Borgmann)
pp. 229–231, 2018.

Magnetic-field-induced Actuation of Ni-Mn-Ga Micropillars

D. Musiienko, Lappeenranta University of Technology, Savonlinna, Finland
L. Straka, L. Klimša
Institute of Physics of the Czech Academy of Sciences, Prague, Czech Republic
A. Saren, A. Sozinov
Lappeenranta University of Technology, Savonlinna, Finland
O. Heczko, Institute of Physics of the Czech Academy of Sciences, Prague, Czech Republic
K. Ullakko, Lappeenranta University of Technology, Savonlinna, Finland

Abstract:
We report on magnetic-field-induced actuation of $Ni_{50}Mn_{28.5}Ga_{21.5}$ single crystalline micropillars. Focused ion beam (FIB) milling technology was used to machine 45×45×120 μm^3 cuboid pillars. The removal of about 2 μm of ion-beam-damaged surface layer enabled magnetic field actuation in pillars. Our results demonstrate the feasibility of manufacturing of microns-sized magnetic shape memory actuators by using Xe plasma source FIB technique.

Keywords: Magnetic Shape Memory, Twinning, Ni-Mn-Ga, Focused Ion Beam, Micro-scale Magnetic Actuation

Introduction

Magnetic shape memory (MSM) alloys are known for exhibiting large reversible magnetic-field-induced strain (MFIS) in the martensite phase [1, 2]. MSM alloys offer prospects for novel applications and embody a unique mechanism for magnetic-to-mechanical energy conversion. Therefore, they were under the scope of scientific research during the past decades [3 – 6]. The mechanism behind the MSM effect is the magnetically induced reorientation (MIR) of the crystal lattice by twin boundary (TB) motion [7, 8]. High velocities of TBs discovered in MSM materials [9] are important for new applications, especially in microscale devices. Thus, scaling down is a natural step in the evolution of MSM actuation devices. Similar to microelectromechanical systems (MEMS), here the key idea is to replace existing complex multi-component systems by magneto-mechanically active materials.

The operation of MSM alloys as shape memory material was previously shown in micro- and nanoactuators: Ni-Mn-Ga beams exhibited reversible thermal and thermomagnetic shape memory effect down to 100 nm [10 – 12]. The operating principle there was based on the martensite-austenite phase transformation induced by heating and/or by magnetic field application. However, to obtain the true advantage of the MSM effect, especially the fast and large actuation simultaneously, MIR must be employed. Thus, MSM microactuators should be based on the single-crystalline material.

Recently, we have shown the feasibility of creation of a magnetically active micropillar by FIB milling technology followed by electro-chemical etching [13]. In the present study, we report on the reversible actuation of MSM micropillar. Bulk Ni-Mn-Ga single crystal used for the pillars milling exhibited five-

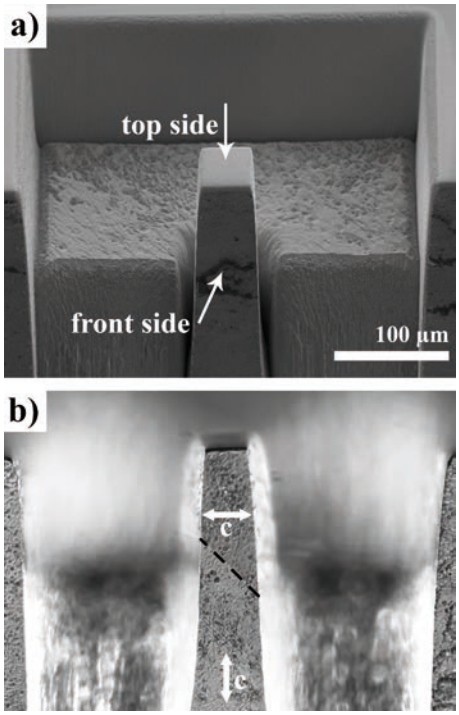

Fig. 1: *(a) Top-front view of the pillar captured by SE detector in SEM after FIB milling procedure and (b) optical micrograph of the side of fully actuated pillar in polarized light. In (a), the top and front sides of the pillar are marked with arrows. In (b), easy magnetisation c-axis orientations of twin variants are denoted by arrows, TB is marked by dashed line. Both images are equally scaled.*

 ISBN 978-3-933339-30-0

layered modulated martensite structure at room temperature. Martensite transformation and Curie temperatures of the crystal were T_M = 321 K, T_A = 327 K and T_C = 371 K, and maximum possible MFIS derived from the lattice parameters was 1 − c/a = 6.3% [14]. Thus, our goal was to achieve strains of more than 6% by application of a magnetic field. Ultimately, the reverse actuation must not involve a mechanical force application to the material.

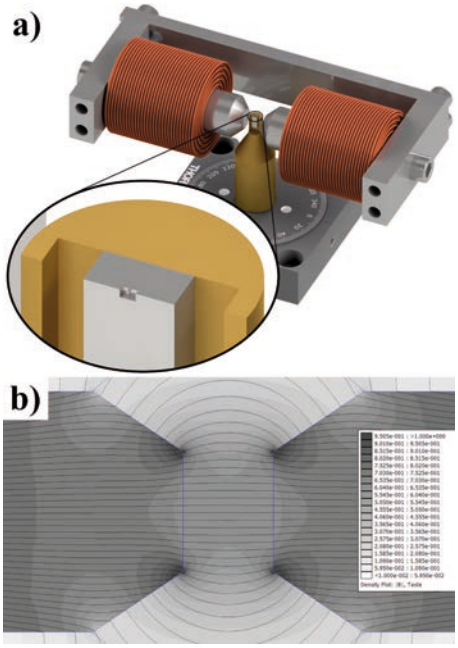

Fig. 2: *(a) Schematic view of the in-house built rotatable sample holder setup equipped with an electromagnet. (b) Magnetic field distribution within the air-gap calculated in Finite Element Method Magnetics package [15].*

Experimental

Fig. 1(a) shows the SEM image of the micropillar after FIB milling with the size of approximately 45×45×120 μm^3. The electro-chemical removal of about 2 μm of ion-beam-damaged surface layer enabled magnetic field actuation of the micropillar [13]. The side view of the sample with magnetically induced twin variant in first possible TB orientation is shown in Fig. 1(b), from which the active length of the pillar was found to be about 100 μm.

Fig. 2(a) represents the schematic view of the in-house built rotatable sample holder setup equipped with an electromagnet. The setup was designed for the direct observation of the pillar response to the applied magnetic field. An electromagnet was capable of creating magnetic fields up to $\mu_0 H$ = 0.65 T within 6 mm long cylindrical air-gap between the concentration poles of 8 mm in diameter. Fig. 2(b) shows the magnetic field distribution at 5 A current within the air-gap calculated in Finite Element Method Magnetics package [15].

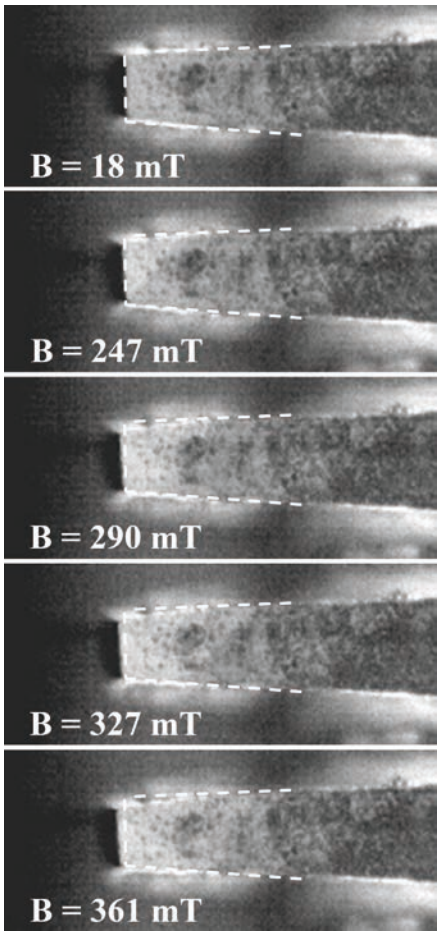

Fig. 3: *Temporally ordered optical micrographs of the MIR of the pillar during the magnetic field sweep. Dashed line denotes initial pillar shape on each frame for the reference.*

Prior to the MIR investigation, the sample with the milled pillar was reoriented to the single-variant state in saturating magnetic field ($\mu_0 H$ = 1.5 T) applied along the pillar longest dimension. It was then glued with a super glue onto the sample holder to ensure that TBs will move only within the pillar and will not be driven by the MIR of twin variants in the bulk. Then the sample holder was oriented in a way that the magnetic field will be applied perpendicularly to the pillar, see Fig. 2(a). The MIR of the pillar was recorded at 30000 frames per second by Photron FASTCAM SA5 model 775K-

ISBN 978-3-933339-30-0

M2 monochrome video camera temporally synchronized with the magnetic field sweep from remanent field of 0.02 T to 0.65 T. Polarized light contrast was used to distinguish TB position.

Results and Discussion

Fig. 3 represents the indicative frames of the footage with corresponding values of applied magnetic field. The TB motion occurs in steps, which is explained by the non-uniform field distribution within the sample [16]. To retrieve the initial state of the pillar (fully contracted) the sample holder was rotated 90°. During the magnetic field sweep TB moved through the entire pillar within less than 0.1 ms when the field reached value of 0.12 T.

Fig. 4: *AFM image of the region of the pillar with the TB, mapped by MFM image. Arrows indicate easy magnetisation c-axis orientation in twin variants. Dashed line denote TB position.*

The second possible TB orientation variant was induced by repeated magnetic field application in another pair of perpendicular directions (a normal to the front and a normal to the top sides of the pillar). Fig. 4 shows Magnetic field microscopy image of the front side of the pillar with the TB in the middle. We observed a branched magnetic domain (MD) structure in the martensite variant with the easy magnetisation axis perpendicular to the surface and a 'needle-like' MD structure in the variant with the c-axis laying in the surface plane [17]. The observed MD structure is inherited from the bulk material [18]. This confirms that magnetic properties of the studied object are similar to those of the bulk.

Conclusions

We presented for the first time the magneto-mechanically active micropillars manufactured from the bulk Ni-Mn-Ga single crystal using standard techniques. The thickness of ion-beam-damaged layer was found to be smaller than 2 µm. Fully reversible MIR of the pillar was shown to be possible. The magnetic fields required for magnetic actuation are below 0.4 T. These important results indicate that FIB milled structures with the scale of several micrometres based on the MSM alloys could be used as micro-magneto-mechanical devices.

Acknowledgements

This work was supported by the Academy of Finland (grant number 287016). This project has received funding from the European Union's Horizon 2020 research and innovation programme under grant agreement No 701867 – FUNMAH. Authors acknowledge the Czech Science Foundation (grant No. 16-00043S) and in part the MEYS CR FUNBIO CZ.2.16/3.1.00/21568 (SEM purchase), LO1409 and LM2015088 projects (SEM maintenance).

References

[1] K. Ullakko, J. Mater. Eng. Perform. 5 (1996) 405.
[2] K. Ullakko, J. K. Huang, C. Kantner, R. C. O'Handley, V. V. Kokorin, Appl. Phys. Lett. 69 (1996) 1966–1968.
[3] A. Sozinov, A. Likhachev, N. Lanska, K. Ullakko, Appl. Phys. Lett. 80 (2002) 1746–1748.
[4] S. J. Murray, M. Marioni, S. M. Allen, R. C. O'Handley, T. A. Lograsso, Appl. Phys. Lett. 77 (2000) 886–888.
[5] D. C. Dunand, P. Müllner, Adv. Mater. 23 (2011) 216–232.
[6] E. Faran, D. Shilo, Exp. Tech. 40 (2016) 1005–1031.
[7] A. A. Likhachev, K. Ullakko, Eur. Phys. J. direct 1 (2000) 1–9.
[8] I. Aaltio, A. Sozinov, Y. Ge, K. Ullakko, V. K. Lindroos, S.-P. Hannula, Ref. Module in Mater. Sci. and Mater. Eng. (2016) 14.
[9] A. Saren, T. Nicholls, J. Tellinen, K. Ullakko, Scr. Mater. 123 (2016) 9–12.
[10] M. Kohl, M. Schmitt, A. Backen, L. Schultz, B. Krevet, S. Fähler, Appl. Phys. Lett. 104 (2014) 043111.
[11] M. Kohl, M. Gueltig, V. Pinneker, R. Yin, F. Wendler, B. Krevet, Micromachines 5 (2014) 1135–1160.
[12] E. Kalimullina, A. Kamantsev, V. Koledov, V. Shavrov, V. Nizhankovskii, A. Irzhak, F. Albertini, S. Fabbrici, P. Ranzieri, P. Ari-Gur, Phys. status solidi (c) 11 (2014) 1023–1025.
[13] D. Musiienko, L. Straka, L. Klimša, A. Saren, A. Sozinov, O. Heczko, K. Ullakko, Scr. Mater. *Accepted for publication on March 14* (2018).
[14] A. Sozinov, N. Lanska, A. Soroka, L. Straka, Appl. Phys. Lett. 99 (2011) 124103.
[15] D. C. Meeker, FEMM Ver. 4.2 x64 (12Jan2016). URL: http://www.femm.info.
[16] O. Heczko, D. Vokoun, V. Kopeck, M. Beleggia, IEEE Magn. Lett. 6 (2015) 1–4.
[17] Y.-W. Lai, R. Schäfer, L. Schultz, J. McCord, Appl. Phys. Lett. 96 (2010) 022507.
[18] O. Heczko, V. Kopecký, L. Fekete, K. Jurek, J. Kopeček, L. Straka, H. Seiner, IEEE Trans. Magn. 51 (2015) 1–4.

ISBN 978-3-933339-30-0

Publication IV

Musiienko, D., Saren, A., Straka, L., Vronka, M., Kopeček, J., Heczko, O., Sozinov, A., Ullakko, K.

Ultrafast actuation of Ni-Mn-Ga micropillars by pulsed magnetic field

Reprinted with permission from
Scripta Materialia
Vol. 162, pp. 482–485, 2019

Scripta Materialia 162 (2019) 482–485

Contents lists available at ScienceDirect

Scripta Materialia

journal homepage: www.elsevier.com/locate/scriptamat

Ultrafast actuation of Ni-Mn-Ga micropillars by pulsed magnetic field

Denys Musiienko[a], Andrey Saren[a], Ladislav Straka[b], Marek Vronka[b], Jaromír Kopeček[b], Oleg Heczko[b], Alexei Sozinov[a], Kari Ullakko[a,*]

[a] Material Physics Laboratory, Lappeenranta University of Technology, Laitaatsillantie 3, Savonlinna 57170, Finland
[b] Institute of Physics of the Czech Academy of Sciences, Na Slovance 2, Prague 8 182 21, Czech Republic

ARTICLE INFO

Article history:
Received 25 September 2018
Received in revised form 12 November 2018
Accepted 5 December 2018
Available online xxxx

Keywords:
Ferromagnetic shape memory
Twinning
Nanoindentation
Focused ion beam
Ni-Mn-Ga micropillars

ABSTRACT

We report on the pulsed magnetic field actuation of single crystalline Ni-Mn-Ga cuboid micropillars with dimensions of 40 × 45 × 120 μm^3, created by focused ion beam milling followed by electrochemical etching. Based on the experimental and modelled results, we differentiate between type I and type II twin boundary motion in the micropillar, which display about an order difference in actuation velocities. Magnetically-induced reorientation of a micropillar was obtained in less than 5 μs by type II twin boundary motion. Our results suggest the possibility of fabrication of magnetic shape memory microdevices with working frequencies up to 100 kHz.

Ni-Mn-Ga off-stoichiometric Heusler compounds are known for the magnetic shape memory (MSM) effect they exhibit in martensitic phase [1]. The MSM effect derives from the MSM material's unique ability to develop giant strains when exposed to a magnetic field that retain their shape after the field is removed [2-4]. Magnetic-field-induced strain (MFIS) in MSM alloys is the result of the magnetically-induced reorientation (MIR) of the crystal lattice caused by the motion of twin boundaries (TBs) [5-7]. Modern development of micro-actuators has inspired numerous studies on the behavior of actuation materials at microscale [8-12]. The MSM alloys were previously used in micro- and nanoactuators as shape memory material: Ni-Mn-Ga beams exhibited reversible thermal and thermomagnetic shape memory effect down to 100 nm [13-15]. Campanini et al. has recently demonstrated magnetic field assisted shape memory effect in free-standing 75 nm thick Ni-Mn-Ga nanodisks [16]. The indication of the existence of MIR in MSM foils was shown in Refs.[17,18]. Recently, we demonstrated giant MFIS in a foil thinned down to 1 μm [19] and in micropillars [20], both fabricated from bulk Ni-Mn-Ga crystals.

The goal of the present work is to investigate MSM actuation kinetics at the microscale. We combined experimental and modelling approaches to explore the difference in mobility of type I and type II TBs in micropillars. The results are compared with those obtained for bulk, mm-sized samples in Refs. [21-23].

Two micropillars were machined using the focused ion beam (FIB) milling technique on two separate single crystalline cuboid samples (6.5 × 2.5 × 1 mm^3) with nominal composition $Ni_{50}Mn_{28.5}Ga_{21.5}$. The FIB milling was performed using fully integrated Xe plasma source FIB using scanning electron microscope (FIB-SEM) TESCAN FERA3 GM. The process was monitored by secondary electrons (SE) imaging (Everhart-Thornley SE detector) at 5 kV / 500 pA for SEM and 30 kV / 10 nA for FIB-generated SE. Rough 100 μm deep milling at 30 kV / 300 nA was followed by more precise pillar polishing at 30 kV / 100 nA. To provide a controlled smooth removal of the surface deformation layer, a custom electropolishing technique was used. An electrolyte mixture of 1 part of 60% HNO_3 and 3 parts of denatured ethanol was kept at 253 K. Pulse width modulated voltage (at 50 Hz) was applied between the sample (anode) and acid-resistant stainless steel spiral (cathode) immersed into the electrolyte solution, which was constantly mixed using a magnetic chemical stirrer [20]. Fig. 1a shows the SEM image of a FIB-milled micropillar after the stress removal treatment. The resultant micropillars had a cuboid shape with typical dimensions of 40 × 45 × 120 μm^3 when the easy magnetization c-axis was oriented along their longest dimension. The magnetically active part of micropillars was found to be about 100 μm long when measured from the top side.

* Corresponding author.
E-mail address: kari.ullakko@lut.fi (K. Ullakko).

https://doi.org/10.1016/j.scriptamat.2018.12.009
1359-6462/

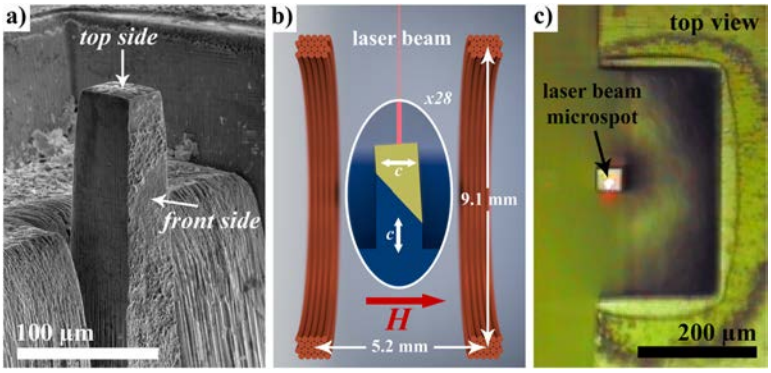

Fig. 1. (a) SEM image of a FIB-milled MSM micropillar after electro-polishing. (b) Schematic cross-sectional front view of the micropillar inside the Helmholtz coil during elongation measurement. The central area of (b) (pictured within the white elliptical frame) is magnified 28 times. The directions of the easy c-axis in different twin variants are marked by the white arrows, and the direction of magnetic field ***H*** is marked by the red arrow. (c) Top view photograph of the micropillar taken with a built-in LDV camera prior to actuation. The LDV laser beam is focused on the top side of the pillar. (For interpretation of the references to color in this figure legend, the reader is referred to the web version of this article.)

For the fast actuation of the micropillars we used a pulsed magnetic field set-up that was initially developed in Ref. [22] for bulk, mm-sized MSM samples. Two coaxial coils connected in series (Helmholtz configuration), were used to generate the magnetic field. Each coil has a diameter of 9.1 mm and consists of 20 turns of an insulated copper wire of 0.2 mm in diameter, with a distance between coils of 5.2 mm (see Fig. 1b). The coils' frame has an axial hole and a few openings between the coils to allow for the positioning of the sample holder and observation the top and front sides of the micropillar. A Polytec OFV-5000, OFV-534 Laser Doppler Vibrometer (LDV), equipped with an additional lens that reduced the spot size down to ~1.5 µm, was used to measure the actuation velocity and displacement of the top side of the pillar. The micropillar's shape change during actuation was monitored from the front side by a Photron FASTCAM SA-Z connected to a microscope (Zeiss Axio Scope.A1). The construction of the sample holder and the system's microscope mount allowed for the 90° rotation of the Helmholtz coil around the sample, providing the possibility for magnetic field application along and perpendicular to the micropillar. Fig. 1b shows the front view of a schematic cross-section of the micropillar inside the coil during the elongation measurement. The central area of the figure (pictured in the white elliptical frame) is magnified to make the micropillar visible against the Helmholtz coil in the background. Fig. 1c shows a representative snapshot taken by the built-in LDV camera after the laser beam was focused on the top side of the pillar. To achieve high-speed camera imaging, the micropillar was illuminated by a CoolLED pE-4000 light source through the microscope's reflected light pathway. Magnetic field strength in the place of the micropillar was calculated from the measured Helmholtz coil current. The pulse circuit was configured to provide a square-like current pulse with a length of ~60 µs and an amplitude of 230 ± 15 A which corresponds to magnetic field of 0.85±0.05 T. Front edge of the pulse was reaching the saturation magnetic field of ~0.6 T in ~2 µs. Details of the LDV measurement set-up and magnetic field pulse generation can be found in Refs. [21,22].

Prior to the TB kinetics investigation, two samples were glued to the sample holders in a single variant state with the easy c-axis oriented along the micropillar. The same acrylic glue was used to cover the free surfaces of the samples to prevent formation of any twin bands within the bulk part. Fig. 2 shows the optical micrographs of the front side of the micropillar in polarized light taken during the representative pair of elongation-contraction measurements for slow-moving TBs. Two twin variants with different orientations of the easy c-axis are distinguishable due to the contrast provided by the polarized light. The initial portion of the second twin variant (see Fig. 2) was introduced by the manual application of a mechanical force ***F*** to the top part of the micropillar in a shear direction. Then magnetic field ***H*** was applied perpendicularly to the micropillar. This resulted in full elongation of the active part of the micropillar. The active part had a length of about 100 µm (see Fig. 2b), which corresponds to the maximum displacement of the micropillar's top of ~6 µm. The contracted state shown in Fig. 2c was achieved by application of the same magnetic field pulse along the micropillar. Introduction of the initial "triangle" of the second twin variant was possible only with the slow-moving TBs. It was not possible to control the position of fast-moving TBs with the manual application of mechanical force as they were too mobile; thus, we manipulated these TBs using a magnetic field. The application of a magnetic field along the micropillar allowed us to move the TB towards the top side and perpendicularly — towards the micropillar's bottom.

Two well-defined actuation velocity patterns were recognized in the samples studied. Fig. 3 shows two representative pairs of elongation-contraction measurements. The absolute value of the displacement of the top side of the micropillar (left ordinate) and the calculated magnetic field values (right ordinate) are plotted as functions of time. The speed difference of about an order allowed us to presume the type of TBs that were propagated during the experiment. Reflecting the similarities in actuation velocity values found earlier for bulk, mm-sized samples [21,23], it was considered that slow-moving TBs were type I TBs and fast-moving TBs were type II. Average actuation velocities were found to be 0.18 m/s for type I TBs and 1.3 m/s for type II TBs, and corresponding TB motion speeds were 2.6 m/s and 20 m/s, respectively. In Fig. 3, it can be seen that the absolute elongation of the micropillar for type I TBs is shorter than its absolute contraction because part of a second variant had already been introduced into the pillar. The difference in absolute displacements for type II TBs was possibly caused by the higher surface stress in the bottom part of the pillar, which pushed back the highly mobile twinning interface.

High-speed camera footage did not show any significant motion of the sample during TB propagation. *Video recordings of the front side of the micropillar during the application of the magnetic field pulse can be found in the supplementary material available online.* This confirms

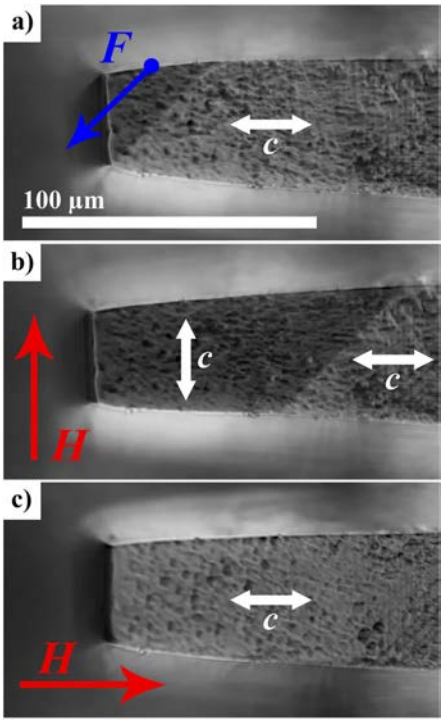

Fig. 2. Optical micrographs of the front side of a micropillar showing the stages of elongation-contraction measurement. Twin variants are differentiated by the optical contrast in polarized light and the easy c-axis orientations are marked by white arrows. (a) Initial state with purposely introduced type I TB. The direction of the mechanical force ***F*** and application point are marked by the blue arrow and dot, respectively. (b) Elongated state after pulsed magnetic field application perpendicular to the micropillar. (c) Contracted state after a magnetic pulse application along the micropillar. (For interpretation of the references to color in this figure legend, the reader is referred to the web version of this article.)

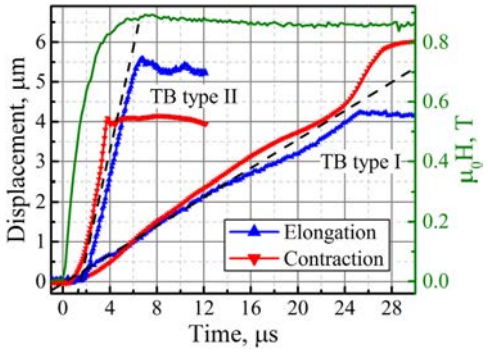

Fig. 3. Two pairs of elongation-contraction measurements showing different actuation velocities, attributed to type I and type II TB motion. The absolute value of the displacement of the top side of the micropillar (left ordinate) and calculated magnetic field (right ordinate) are plotted versus time. The dashed lines represent the linear fits for displacements, the slopes of which provide actuation velocity values of 0.18 m/s for type I TB and of 1.3 m/s for type II.

that the recorded LDV signals are related to TB motion within the micropillar's active part only. We observed uniform shape change of the micropillar under exposure to a magnetic field pulse, which strongly suggests the possibility of single TB motion. Observed shape change times correspond with the measured displacement data for the top side of the micropillar.

Observed TB velocities are approximately 40% lower than in the bulk, mm-sized samples (4.2 m/s for type I TBs and 33 m/s for type II [21]). To determine the reason for such behavior, we employed the flat punch indenter to measure the twinning stress (TS) required to move TBs of different types. We used a custom-made boron-doped diamond punch, with a diameter of 20 µm at its flat end, to push the micropillar from the top side. Prior to each measurement, the micropillar was fully elongated in a magnetic field (as shown in Fig. 2b). The process was monitored by scanning electron microscope (SEM) to ensure that only a single TB was being moved. Compression of the micropillar was performed using a Hysitron PI 85 SEM PicoIndenter inside a FEI Quanta 3D FEG Dual Beam SEM. An Everhart Thornley detector was used to capture electron micrographs of the micropillar during the compression process. Errors in force and displacement measurement were 400 nN and 1 nm, respectively. We succeeded in recording multiple TS measurements for TBs of different types. For type I TBs, we recorded an average value of 2.3 ± 0.3 MPa and an average value of 0.8 ± 0.15 MPa for type II. These TS values are less than the magnetic stress developed by the material in the saturating magnetic field (a typical σ_{mag} is about 3 MPa for the used composition [24]), which ensures the feasibility of the MSM effect in Ni-Mn-Ga micropillars. Details of the TS measurement procedure used can be found in Supplementary A. *An example of the SEM continuous scan video is available on-line*. According to the literature, five-layered Ni-Mn-Ga single crystals demonstrate TS values of ~1 MPa for type I TBs and ~0.05–0.3 MPa for type II TBs [25,26]. One of the reasons for the increased TS in the micropillars could be that the surface stresses inflicted by FIB milling were not fully removed by the electrochemical etching. At the same time, we might be approaching the size limitation for the MIR [10]. However, this issue requires further investigation, including fabrication of MSM microstructures of different sizes, and refinement of the surface removal technique.

The present study utilized the macroscopic variable-mass model describing single TB motion and developed in Ref. [23]. The model takes into account the mass inertia of the moving variant and assumes TB velocity-dependent or dynamic twinning stress. Similar to Ref. [23], the dynamic TS for type I TB was modelled as $\sigma_1 = 2.0 + 0.4 \times V_{TB}$ (MPa), and for type II TB – as $\sigma_2 = 0.9 + 0.026 \times V_{TB}^{1.4}$ (MPa), where V_{TB} is TB velocity. Here, the static TS values correspond to the measured compressive TS, and dynamic stress coefficients were adjusted according to the average saturation TB velocity values (see Supplementary B for further details). Fig. 4 shows the measured and modelled micropillar elongation velocity and corresponding single TB motion speed for type I (a) and type II TBs (b). The delay of about 1 µs for type II TB was most probably caused by extra surface stresses in the top corner of the micropillar, from which the twinning interface starts its motion. Additionally, it includes the time it takes the TB to cross the laser beam in order to be detected. It should be noted that, in accordance with the model, the acceleration times required to reach saturation velocity were significantly lower for both types of TBs in the case of micropillars as compared with the mm-sized samples due to the decrease of moving mass. This is seen most clearly in type II TB, for which the acceleration time is about 2 µs for micropillars, whereas for mm-sized samples it is ~ 20 µs [23]. The model suggests a pronounced scaling effect. This effect

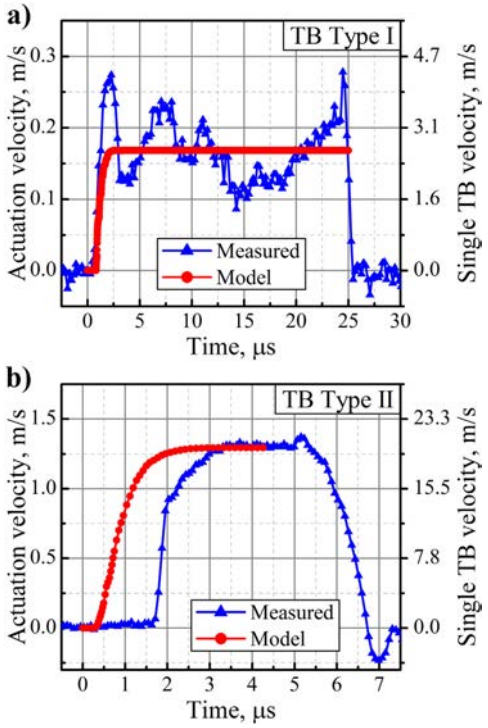

Fig. 4. Measured and modelled micropillar elongation velocity (left ordinate) versus time for pulsed magnetic field actuation of type I (a) and type II (b) TBs. The right ordinates show corresponding TB velocity scales. Please note the difference in time and velocity scales between (a) and (b).

occurs because the driving force scales proportionally to the dimension in squared units whereas the mass scales proportionally to the dimension in cubed units. From the model, it follows that the initial acceleration for a smaller sample will increase nearly proportionally to the sample's dimension, which leads to a proportionally shorter acceleration time before the velocity saturates. Thus, the observed fast, 5 μs-scale actuation of the micropillars is a result of both the high mobility of type II TBs and the scaling effect.

In conclusion, we report, for the first time, on the pulsed magnetic-field-induced actuation of Ni-Mn-Ga single crystalline micropillars. We find evidence of a difference in dynamics for type I and type II twin boundaries at the microscale. The measured actuation velocities of 0.18 and 1.3 (m/s) for type I and type II twin boundaries, respectively, correspond to twin boundary propagation speeds of 2.6 and 20 (m/s) for type I and type II twin boundaries, respectively. These findings correspond strongly with the previously reported values for single twin boundary motion in bulk, mm-sized samples. Twinning stresses for single twin boundaries motion in micropillars were revealed to be ~2.3 MPa for type I twins and ~0.8 MPa for type II. We suggest that increased twinning stress values (in comparison to the values for bulk material) are related to the incomplete removal of surface defects, but this issue requires further investigation. The actuation acceleration of micropillars is approximately an order of magnitude larger than in bulk samples, demonstrating a well-pronounced scaling effect connected to the decrease of cross-section in actuated MSM crystals and therefore the reduction of moving mass. It is shown that the complete magnetically-induced reorientation of the active length of 100 μm of the micropillar can be obtained in about 5 μs for type II twin boundary. Our results suggest the possibility of fabricating MSM-based microdevices with working frequencies of 100 kHz.

Acknowledgments

We would like to acknowledge Ladislav Klimša for his expertise in the FIB milling and SEM imaging. This work was supported by the Academy of Finland (grant number 287016). This project has received funding from the European Union's Horizon 2020 - Research and Innovation Framework Programme under grant agreement No 701867 – FUNMAH. This work was supported by the project LM2015087 of the Czech Ministry of Education, Youth and Sports. Authors acknowledge the Czech Science Foundation (grant No. 16-00043S) and in part the MEYS CR FUNBIO CZ.2.16/3.1.00/21568 (SEM purchase), LO1409 and LM2015088 projects (SEM maintenance).

Appendix A. Supplementary data

Supplementary data to this article can be found online at https://doi.org/10.1016/j.scriptamat.2018.12.009.

References

[1] K. Ullakko, J.K. Huang, C. Kantner, R.C. O'handley, V.V. Kokorin, Appl. Phys. Lett. 69 (1996) 1966–1968.
[2] R. Tickle, R. James, J. Magn. Magn. Mater. 195 (1999) 627–638.
[3] S.J. Murray, M. Marioni, S.M. Allen, R.C. O'handley, T.A. Lograsso, Appl. Phys. Lett. 77 (2000) 886–888.
[4] H. Karaca, I. Karaman, B. Basaran, Y.I. Chumlyakov, H. Maier, Acta Mater. 54 (2006) 233–245.
[5] S.A. Wilson, R.P. Jourdain, Q. Zhang, R.A. Dorey, C.R. Bowen, M. Willander, Q.U. Wahab, S.M. Al-hilli, O. Nur, E. Quandt, et al. Mater. Sci. Eng. R. Rep. 56 (2007) 1–129.
[6] O. Heczko, N. Scheerbaum, O. Gutfleisch, Nanoscale Magnetic Materials and Applications, Springer, Boston, MA, 2009, pp. 399–439. https://doi.org/10.1007/978-0-387-85600-1_14.
[7] M. Acet, L. Mañosa, A. Planes, Handbook of Magnetic Materials, vol. 19, Elsevier. 2011, pp. 231–289.
[8] C. Jenkins, R. Ramesh, M. Huth, T. Eichhorn, P. Pörsch, H. Elmers, G. Jakob, Appl. Phys. Lett. 93 (2008) 234101.
[9] M. Reinhold, D. Kiener, W.B. Knowlton, G. Dehm, P. Müllner, J. Appl. Phys. 106 (2009) 053906.
[10] D.C. Dunand, P. Müllner, Adv. Mater. 23 (2011) 216–232.
[11] J.M. Jani, M. Leary, A. Subic, M.A. Gibson, Mater. Des. (1980-2015) 56 (2014) 1078–1113.
[12] E. Faran, D. Shilo, Exp. Tech. 40 (2016) 1005–1031.
[13] M. Kohl, M. Schmitt, A. Backen, L. Schultz, B. Krevet, S. Fähler, Appl. Phys. Lett. 104 (2014) 043111.
[14] M. Kohl, M. Gueltig, V. Pinneker, R. Yin, F. Wendler, B. Krevet, Micromachines 5 (2014) 1135–1160.
[15] E. Kalimullina, A. Kamantsev, V. Koledov, V. Shavrov, V. Nizhankovskii, A. Irzhak, F. Albertini, S. Fabbrici, P. Ranzieri, P. Ari-Gur, Phys. Status Solidi C 11 (2014) 1023–1025.
[16] M. Campanini, L. Nasi, S. Fabbrici, F. Casoli, F. Celegato, G. Barrera, V. Chiesi, E. Bedogni, C. Magén, V. Grillo, et al. Small (2018) 1803027.
[17] M. Thomas, O. Heczko, J. Buschbeck, U. Rößler, J. McCord, N. Scheerbaum, L. Schultz, S. Fähler, New J. Phys. 10 (2008) 023040.
[18] P. Ranzieri, M. Campanini, S. Fabbrici, L. Nasi, F. Casoli, R. Cabassi, E. Buffagni, V. Grillo, C. Magén, F. Celegato, et al. Adv. Mater. 27 (2015) 4760–4766.
[19] D. Musiienko, A. Saren, K. Ullakko, Scr. Mater. 139 (2017) 152–154.
[20] D. Musiienko, L. Straka, L. Klimsa, A. Saren, A. Sozinov, O. Heczko, K. Ullakko, Scr. Mater. 150 (2018) 173–176.
[21] A. Saren, D. Musiienko, A. Smith, K. Ullakko, Scr. Mater. 113 (2016) 154–157.
[22] A. Saren, T. Nicholls, J. Tellinen, K. Ullakko, Scr. Mater. 123 (2016) 9–12.
[23] A. Saren, K. Ullakko, Scr. Mater. 139 (2017) 126–129.
[24] I. Aaltio, A. Sozinov, Y. Ge, K. Ullakko, V.K. Lindroos, S.-P. Hannula, Ref. Module in Mater. Sci. and Mater. Eng. (2016).
[25] L. Straka, O. Heczko, H. Seiner, N. Lanska, J. Drahokoupil, A. Soroka, S. Fähler, H. Hänninen, A. Sozinov, Acta Mater. 59 (2011) 7450–7463.
[26] A. Sozinov, N. Lanska, A. Soroka, L. Straka, Appl. Phys. Lett. 99 (2011) 124103.

ACTA UNIVERSITATIS LAPPEENRANTAENSIS

802. JÄRVI, HENNA. Customer engagement, a friend or a foe? Investigating the relationship between customer engagement and value co-destruction. 2018. Diss.

803. DABROWSKA, JUSTYNA. Organizing for open innovation: adding the human element. 2018. Diss.

804. TIAINEN, JONNA. Losses in low-Reynolds-number centrifugal compressors. 2018. Diss.

805. GYASI, EMMANUEL AFRANE. On adaptive intelligent welding: Technique feasibility in weld quality assurance for advanced steels. 2018. Diss.

806. PROSKURINA, SVETLANA. International trade in biomass for energy production: The local and global context. 2018. Diss.

807. DABIRI, MOHAMMAD. The low-cycle fatigue of S960 MC direct-quenched high-strength steel. 2018. Diss.

808. KOSKELA, VIRPI. Tapping experiences of presence to connect people and organizational creativity. 2018. Diss.

809. HERALA, ANTTI. Benefits from Open Data: barriers to supply and demand of Open Data in private organizations. 2018. Diss.

810. KÄYHKÖ, JORMA. Erityisen tuen toimintaprosessien nykytila ja kehittäminen suomalaisessa oppisopimuskoulutuksessa. 2018. Diss.

811. HAJIKHANI, ARASH. Understanding and leveraging the social network services in innovation ecosystems. 2018. Diss.

812. SKRIKO, TUOMAS. Dependence of manufacturing parameters on the performance quality of welded joints made of direct quenched ultra-high-strength steel. 2018. Diss.

813. KARTTUNEN, ELINA. Management of technological resource dependencies in interorganizational networks. 2018. Diss.

814. CHILD, MICHAEL. Transition towards long-term sustainability of the Finnish energy system. 2018. Diss.

815. NUTAKOR, CHARLES. An experimental and theoretical investigation of power losses in planetary gearboxes. 2018. Diss.

816. KONSTI-LAAKSO, SUVI. Co-creation, brokering and innovation networks: A model for innovating with users. 2018. Diss.

817. HURSKAINEN, VESA-VILLE. Dynamic analysis of flexible multibody systems using finite elements based on the absolute nodal coordinate formulation. 2018. Diss.

818. VASILYEV, FEDOR. Model-based design and optimisation of hydrometallurgical liquid-liquid extraction processes. 2018. Diss.

819. DEMESA, ABAYNEH. Towards sustainable production of value-added chemicals and materials from lignocellulosic biomass: carboxylic acids and cellulose nanocrystals. 2018. Diss.

820. SIKANEN, EERIK. Dynamic analysis of rotating systems including contact and thermal-induced effects. 2018. Diss.

821. LIND, LOTTA. Identifying working capital models in value chains: Towards a generic framework. 2018. Diss.

822. IMMONEN, KIRSI. Ligno-cellulose fibre poly(lactic acid) interfaces in biocomposites. 2018. Diss.

823. YLÄ-KUJALA, ANTTI. Inter-organizational mediums: current state and underlying potential. 2018. Diss.

824. ZAFARI, SAHAR. Segmentation of partially overlapping convex objects in silhouette images. 2018. Diss.

825. MÄLKKI, HELENA. Identifying needs and ways to integrate sustainability into energy degree programmes. 2018. Diss.

826. JUNTUNEN, RAIMO. LCL filter designs for paraller-connected grid inverters. 2018. Diss.

827. RANAEI, SAMIRA. Quantitative approaches for detecting emerging technologies. 2018. Diss.

828. METSO, LASSE. Information-based industrial maintenance - an ecosystem perspective. 2018. Diss.

829. SAREN, ANDREY. Twin boundary dynamics in magnetic shape memory alloy Ni-Mn-Ga five-layered modulated martensite. 2018. Diss.

830. BELONOGOVA, NADEZDA. Active residential customer in a flexible energy system - a methodology to determine the customer behaviour in a multi-objective environment. 2018. Diss.

831. KALLIOLA, SIMO. Modified chitosan nanoparticles at liquid-liquid interface for applications in oil-spill treatment. 2018. Diss.

832. GEYDT, PAVEL. Atomic Force Microscopy of electrical, mechanical and piezo properties of nanowires. 2018. Diss.

833. KARELL, VILLE. Essays on stock market anomalies. 2018. Diss.

834. KURONEN, TONI. Moving object analysis and trajectory processing with applications in human-computer interaction and chemical processes. 2018. Diss.

835. UNT, ANNA. Fiber laser and hybrid welding of T-joint in structural steels. 2018. Diss.

836. KHAKUREL, JAYDEN. Enhancing the adoption of quantified self-tracking wearable devices. 2018. Diss.

837. SOININEN, HANNE. Improving the environmental safety of ash from bioenergy production plants. 2018. Diss.

838. GOLMAEI, SEYEDMOHAMMAD. Novel treatment methods for green liquor dregs and enhancing circular economy in kraft pulp mills. 2018. Diss.

839. TEHRANI, MOHAMMAD GERAMI. Mechanical design guidelines of an electric vehicle powertrain. 2019. Diss.

Acta Universitatis
Lappeenrantaensis
840

LUT University

ISBN 978-952-335-334-3
ISBN 978-952-335-335-0 (PDF)
ISSN-L 1456-4491
ISSN 1456-4491
Lappeenranta 2019